

# Hydrogenated Indium Oxide (IO:H) for Thin Film Solar Cell

Ariyanto Wibowo Setia Budhi

MSc Thesis

# Hydrogenated Indium Oxide (IO:H) TCO for Thin Film Solar Cell

By

**Ariyanto Wibowo Setia Budhi**

A thesis submitted for the degree of :

Master of Science in Sustainable Energy Technology

Delft University of Technology

Defended on October 31<sup>st</sup>, 2016

## **Supervisors:**

Dr. Olindo Isabella

Dr. Andrea Illiberi

## **Thesis Comitee:**

Prof. Dr. A.H.M. Smets

Dr. Olindo Isabella

Dr. Andrea Illiberi

Dr. S. W. H. Eijt

# Abstract

Achieving high efficiency solar cells becomes more interesting in order to make solar cell become cost competitive to the other renewable energy sources. Transparent conductive oxide (TCO) which has a requirement to be chemically stable, high transparency and high conductivity, and also application for light trapping application makes it important to be developed. TCO that are commonly used for thin film solar cell has a similar problem, which is high absorption in the near infra-red (NIR) region. Recently, hydrogenated indium oxide (IO:H) has been developed and gained more attention due to the possibility to obtain high mobility with low absorption from visible to NIR region. Therefore the objective of this thesis is the development of high mobility IO:H TCO for thin film solar cells application.

Several parameters have been adjusted in the development of IO:H such as partial pressure of water vapor, thickness, annealing temperature and power. Introduction of water vapor during the deposition suppresses the growth of  $\text{In}_2\text{O}_3$  crystal and make the layer amorphous. Deposition amorphous layer is important to achieve high mobility due to the possibility of defects clustering (oxygen vacancies and indium vacancies) during the annealing. Another important role of water vapor is as the source of hydrogen atoms which could passivate the defects inside IO:H layers. IO:H with mobility of around  $150 \text{ cm}^2/\text{Vs}$  and sheet resistance of  $28 \text{ } \Omega/\square$  (thickness of 100nm) has been developed. By increasing the thickness of IO:H layer, the sheet resistance could be decreased until  $12.5 \text{ } \Omega/\square$  at 400nm thickness with maintaining mobility of  $120 \text{ cm}^2/\text{Vs}$ .

Application of IO:H as TCO in thin film solar cells need to be optimized further. CIGS solar cell with IO:H on top of it indicates a lower efficiency (11.92 %) compared to CIGS with AZO (15.05 %). The loss in CIGS solar cell with IO:H on top of it mainly caused by the drop in the  $V_{\text{OC}}$  and FF of the solar cell. Meanwhile, the a-Si solar cell with IO:H indicates a better efficiency (5.71 %) compared to cell with AZO (5.34%). It gain higher  $V_{\text{OC}}$  and  $J_{\text{SC}}$  but loose in FF. In general the solar cell with IO:H as TCO layer indicates lower FF and higher  $J_{\text{SC}}$  compared to solar cell with AZO.

# Table of Contents

<b>Abstract .....</b>	<b>i</b>
<b>Table of Contents.....</b>	<b>ii</b>
<b>List of Figures .....</b>	<b>v</b>
<b>List of Tables.....</b>	<b>vii</b>
<b>CHAPTER 1 Introduction.....</b>	<b>1</b>
1.1. World Energy Problem .....	1
1.2. Photovoltaic .....	2
1.3. Transparent Conductive Oxide (TCO) .....	2
1.4. TCO Application in Solar Cells.....	3
1.5. Hydrogen doped Indium Oxide (IO:H) .....	4
1.6. Objective .....	4
<b>CHAPTER 2 Physics, Synthesis, and Characterization of TCO .....</b>	<b>7</b>
2.1. Physics of TCO .....	7
2.2. Synthesis of IO:H.....	10
<b>Chapter 3 IO:H Development .....</b>	<b>13</b>
3.1. Basic Sputtering Process.....	13
3.1.1. Effect of Power on Deposition Rate .....	13
3.1.2. Effect of Partial Pressure of Water on Deposition Rate .....	13
3.1.3. Uniformity of the Layer.....	14
3.2. Water Vapor Effect on IO:H layer.....	15
3.2.1. Electrical Properties.....	15
3.2.2. XRD Characterization .....	18
3.2.3. Raman Spectroscopy Characterization.....	23
3.2.4. Optical Properties .....	23
3.2.5. Positron Annihilation Spectroscopy .....	27
3.3. Effect of Annealing Temperature .....	30

3.3.1. Electrical Properties.....	30
3.3.2. XRD Characterization .....	31
3.4. Thickness Effect on IO:H Layer .....	33
3.3.1. Electrical Properties.....	33
3.3.2. XRD Characterization .....	34
3.5. Conclusion .....	37
<b>CHAPTER 4 Application of IO:H on Thin Film Solar Cells .....</b>	<b>39</b>
4.1. CIGS Solar cells.....	39
4.1.1. Basic Test Layer .....	39
4.1.2. Annealing Effect on CIGS Solar Cells .....	41
4.1.3. Effect of ITO .....	42
4.2. Amorphous Silicon Solar Cells.....	43
4.3. Conclusion .....	44
<b>CHAPTER 5 Conclusion and Recommendation .....</b>	<b>45</b>
5.1. Conclusion .....	45
5.2. Recommendation .....	46
<b>References.....</b>	<b>47</b>
<b>Acknowledgements .....</b>	<b>51</b>
<b>Appendix A Characterization Setup.....</b>	<b>53</b>
A.1. Hall Setup .....	53
A.2. Four Point Probe.....	54
A.3. Spectroscopy Ellipsometry .....	55
A.4. Reflectance and Transmittance.....	57
A.5. X-ray Diffraction .....	58
A.6. Raman Spectroscopy .....	59
A.7. Solar Simulator .....	60
A.8. External Quantum Efficiency .....	60

A.9.	Photon Annihilation Spectroscopy (PAS) .....	62
<b>Appendix B Electrical Properties of IO:H layer for different Power .....</b>		<b>65</b>
<b>Appendix C Water vapor effect on different thickness of IO:H .....</b>		<b>67</b>
C.1.	IO:H Layer with 200nm Thickness .....	67
C.2.	IO:H Layer with 400nm Thickness .....	70

## List of Figures

Figure 1. Renewable energy potential on the scale of global energy need [1].....	1
Figure 2. a. CIGS solar cell[8] b. a-si solar cells[9] c. Perovskite solar cell[10] d. HIT solar cell[11] .....	3
Figure 3. Scattering mechanisms in the TCO.....	8
Figure 4. Schematic of charge transport at the grain boundaries [19].....	9
Figure 5. Sputtering setup for IO:H deposition .....	11
Figure 6. Deposition rate at different powers .....	13
Figure 7. Deposition rate for different partial pressure of water .....	14
Figure 8.a. Different thickness of the IO:H layer on top of 10 x 10 cm corning glass. b.Different resistivity of IO:H layer on top of 10 x 10 cm corning glass. ....	14
Figure 9.a. Mobility of IO:H layer with different partial pressure of water. b. Carrier density of IO:H layer with different partial pressure of water. ....	15
Figure 10.a. Resistivity of IO:H layer with different partial pressure of water. b. Sheet Resistance of IO:H layer with different partial pressure of water. ....	16
Figure 11.a. XRD results for as-deposited IO:H layers with different partial pressure of water. b. XRD results for annealed IO:H layers with different partial pressure of water.....	19
Figure 12. Raman setup for annealed IO:H layer with 100nm and 400nm thickness. Inset : BCC structure of defect free $\text{In}_2\text{O}_3$ crystal [31] .....	23
Figure 13. Transmittance and Reflectance of IO:H layer. Inset : Transmittance between 250nm-400nm. ....	24
Figure 14. Absorption coefficient of IO:H layer with different partial pressure of water ..	25
Figure 15.Result of n and k from IO:H layer. Insert : k value for wavelength 200nm to 450nm.....	27
Figure 16.a. Normalized developed IO:H layer with Bulk $\text{In}_2\text{O}_3$ crystal. b. Normalized IO:H layer zoomed in.....	28
Figure 17.a. Mobility and b.carrier density of IO:H layer with different annealing temperature.....	30
Figure 18. Resistivity of IO:H layer with different annealing temperature.....	31
Figure 19. XRD characterization of IO:H layer with different annealing temperature.....	32
Figure 20.a. Mobility and b. Carrier density of IO:H layer for different thickness .....	33
Figure 21.a.Resistivity and b.Sheet resistance of IO:H layer for different thickness.....	34

Figure 22. XRD characterization for sample with different thickness a. as-deposited and b. annealed .....	35
Figure 23.a. Reference CIGS structure b. CIGS with IO:H as TCO.....	39
Figure 24. J-V curve and EQE measurement of CIGS solar cells with different TCO.....	40
Figure 25. J-V curve and EQE measurement of CIGS solar cell with annealed and as deposited IO:H layer .....	41
Figure 26. CIGS with IO:H and ITO as TCO.....	42
Figure 27. J-V curve and EQE measurement of CIGS solar cell with ITO intermediate layer.....	42
Figure 28. a-Si:H solar cell structure with a. AZO and b. IO:H as front TCO.....	43
Figure 29. a. J-V curve and EQE result of a-Si:H solar cell with different TCO.....	44
Figure 30. Scheme of Hall voltage measurement with both positive and negative polarity current, both magnetic field up and down, and both configuration [38] .....	54
Figure 31. Scheme of four-point collinear probe [39].....	55
Figure 32. Scheme of Spectroscopic Ellipsometry [42] .....	56
Figure 33. Ideal reflection and transmission[43].....	57
Figure 34. Scheme of spectrophotometer with integrating sphere[44] .....	58
Figure 35. Geometry of XRD instrument [45] .....	59
Figure 36. Schematic of EQE measurement.....	61
Figure 37. Schematic process in Positron generation from Sodium decay [47].....	62
Figure 38. Illustration of Photon Annihilation spectroscopy measurement [48] .....	63
Figure 39. Mobility, carrier density, and resistivity of IO:H layer for different power .....	66
Figure 40. a. Mobility and b. Carrier density of IO:H layer with thickness of 200nm for different partial pressure of water .....	67
Figure 41. Resistivity and sheet resistance of IO:H layer with thickness of 200nm for different partial pressure of water .....	68
Figure 42. XRD characterization of IO:H layer with thickness of 200nm for different partial pressure of water a. as deposited and b. annealed .....	69
Figure 43. a. Mobility and b. carrier density of IO:H layer with thickness of 400nm for different partial pressure of water .....	70
Figure 44. a. Resistivity and b. sheet resistance of IO:H layer with thickness of 400nm for different partial pressure of water .....	71
Figure 45. XRD characterization for IO:H layer with 400nm thickness with different partial pressure of water a. as-deposited and b. annealed .....	72

## List of Tables

Table 1. Comparison between ITO, AZO, IO:H .....	10
Table 2. Result of XRD calculation.....	21
Table 3. Calculation result of Bandgap and value of n at wavelength 598nm and 1000nm	26
Table 4. Calculation of IO:H for different annealing temperature .....	31
Table 5. XRD calculation for IO:H layer with different thickness .....	36
Table 6. Result of CIGS solar cell with different TCO .....	40
Table 7. Result of annealing CIGS solar cell .....	41
Table 8. Result of CIGS solar cell with ITO intermediate layer .....	43
Table 9. Application of IO:H on a-Si solar cell.....	44
Table 10. XRD calculation for IO:H layer with thickness of 200nm.....	70
Table 11. XRD calculation for IO:H layer with 400nm thickness .....	73

# CHAPTER 1

## Introduction

### 1.1. World Energy Problem

From COP 21 in Paris, it was clearly stated that most of the country in the world agreed that the world should reduce total carbon emission to keep the increase of temperature below 2°C, even urge to improve the standard to keep the limit of temperature increase by 1.5°C. The biggest carbon emission is contributed from the energy sector, mostly by the use of fossil fuels for power generation, which could lead the power generation from renewable energy becomes attractive. Another reason that renewable would energy become more attractive is because the price of electricity generated from renewable energy become cost-competitive with electricity generated from fossil fuels. Figure 1 shows the energy potential of some renewable energy sources on the scale of global energy needs. It could be seen that renewable energy sources have the capabilities to become the main energy source of the world. Another factor that makes renewable energy sources become more important is the increasing of global energy consumption, which makes alternatives energy sources become interesting.

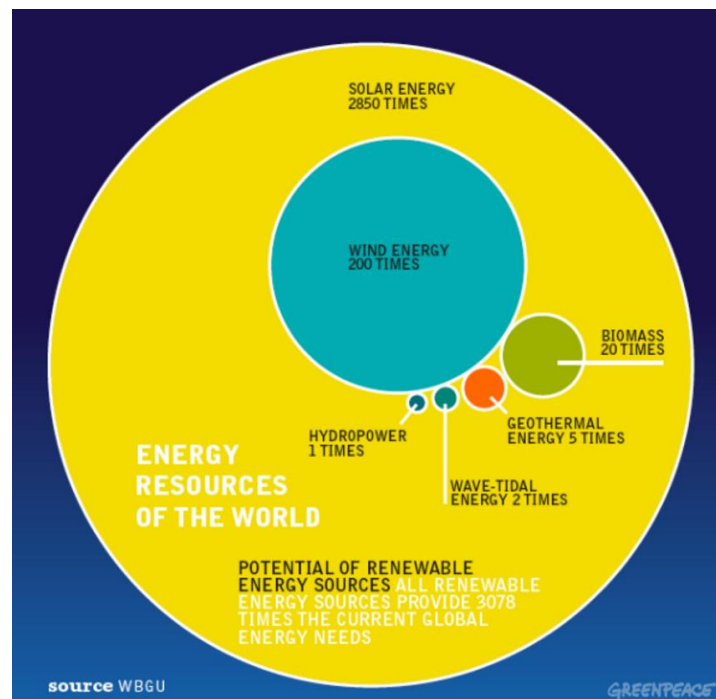


Figure 1. Renewable energy potential on the scale of global energy need [1]

## 1.2. Photovoltaic

Photovoltaic (PV) is an effect which converts sunlight into electricity with a help of a device called solar cell. More than 90% of solar cell market share in the world is dominated by crystalline silicon solar cells. New challenges to lower the price and increase the efficiency of the solar cell have been studied for last decades resulting in thin film solar cells. Thin film solar cells, which are different from crystalline silicon solar cells that need high quality and thick absorber materials, could reduce the cost of solar cells significantly. Since the absorber materials in thin-film solar cells are thinner than crystalline silicon solar cells, the absorption in Infrared (IR) region also decreases. Almost all of the thin film solar cells have one thing in common, which is the transparent conductive oxide (TCO) layer. One thing that needed to be taken into account in the process of designing thin film solar cells is the TCO layer.

## 1.3. Transparent Conductive Oxide (TCO)

Transparent conductive oxides (TCO) are a group of materials which have special properties to be both transparent and electrically conductive [2]. In last three or four decades, TCO has been used in thin film solar cells application, but nowadays, the application of TCO become wider, for example the application in liquid crystal display (LCD) or light emitting diode (LED) [3]. Besides for optoelectronic application, the broader application of TCO such as for architectural and automotive window as prevention of water along the crud condensation on windows, self-cleaning and as a super hydrophobic layer has been developed [4]. There are no exact rules which could conclude the most suitable metal-oxides for formation of TCO, but only empirical rules for dopant. However the experimental result of performance and application of TCO had been gotten [2]. Some examples of metal-oxides that are commonly used as TCO when doped with, either intrinsic or extrinsic, dopants are indium oxide ( $\text{In}_2\text{O}_3$ ), tin oxide ( $\text{SnO}_2$ ), cadmium oxide ( $\text{CdO}$ ), and zinc oxide ( $\text{ZnO}$ ). The most well-known TCO which has good conductivity and high transparenance is tin-doped Indium oxide ( $\text{In}_2\text{O}_3 : \text{Sn}$ ) [2]. Alternatives TCO that have been developed recently are aluminum-doped zinc oxide (AZO) and gallium-doped zinc oxide (GZO). These two TCO become interesting to be developed because they do not use Indium as the based material [5]. Stable supply of Indium might have a problem in the future. It might be caused by the cost and scarcity of Indium that might lead into a problem assuming that optoelectronic market is expanding [6]. Another TCO that has been developed recently is hydrogen-doped Indium Oxide ( $\text{In}_2\text{O}_3 : \text{H}$ ), which

has high mobility of carrier that could reduce the free carrier absorption that leads into higher transparency in near-infrared (NIR) region [7]. Explanation about these phenomena would be explained in Chapter 2.1.

#### 1.4. TCO Application in Solar Cells

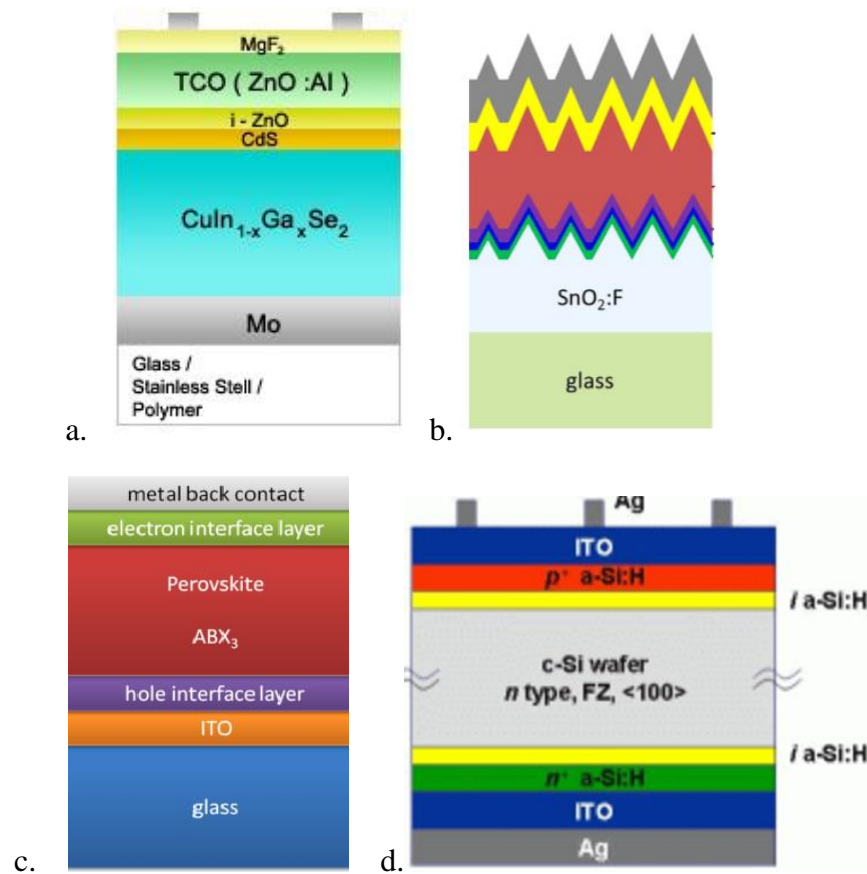


Figure 2. a. CIGS solar cell[8] b. a-si solar cells[9] c. Perovskite solar cell[10] d. HIT solar cell[11]

Figure 2 shows different kinds of TCO application for solar cells. There is an increasing effort to make both low-cost and high-efficiency solar cells. All of these technologies use TCO as one of the basic structures. These solar cells are normally based on the use of new lower costs semiconductors, thin-films of conventional semiconductors, organic-inorganic hybrids, and many other materials. Every solar cell has its own requirements of TCO which leads to further research. For instance, heterojunction with intrinsic thin layer cell (HIT) needs TCOs that have smooth and good interfacial properties, low temperature processing and light trapping. The other example is Copper Indium Gallium Selenide (CIGS) solar cells need TCOs that have interfacial stability to CdS, low temperature deposition, and resistance to diffusion and shunting. Last example is TCOs for amorphous silicon (a-Si:H) solar cells, which should be temperature stable, chemically stable, and have appropriate texture for both TCO layers. Nowadays, the TCO layer

becomes more important than before, since it is not just about conductivity and transparency anymore. For example, TCO could be used as diffusion barriers, control of the contact work function, interface between organic and other materials, and even as a light trapper. Low process temperatures and high process stability become very critical for certain devices. The importance of performance improvements and the increasing price of Indium push the research toward new TCOs for PV application.[12]

### **1.5. Hydrogen doped Indium Oxide (IO:H)**

Hydrogen doped Indium Oxide (IO:H) for TCO was reported first time by Koida in 2007, even though the usage of  $\text{In}_2\text{O}_3$  is already common for TCO application.  $\text{In}_2\text{O}_3$  doped with Tin, commonly known as ITO, is widely used for LED or solar cells. ITO has a typical value of mobility 20-40  $\text{cm}^2/\text{Vs}$  and carrier density of  $10^{19}$ - $10^{21} \text{ cm}^{-3}$  depending on the thickness and film composition[13]. Koida shows that hydrogen doped indium oxide could obtain value of mobility exceeding 100  $\text{cm}^2/\text{Vs}$  with carrier density of  $10^{20} \text{ cm}^{-3}$  which results in a good transparency in the NIR region [14]. These properties make IO:H an advantageous material to replace or improve ITO, especially if the sensitivity in NIR region is needed [15]. Most behavior of the semiconductor interstitial hydrogen atoms ( $\text{H}_i$ ) act is amphoteric, which means it acts as a donor in p-type semiconductors and as an acceptor in n-type semiconductors. This characteristic of  $\text{H}_i$  causes self-compensates in conductivity. But there are some exceptions, such as in ZnO, hydrogen atoms act as unintentional n-type conductivity. So does for  $\text{In}_2\text{O}_3$ ,  $\text{H}_i$  acts as shallow donor which also could be result in n-type conductivity. Moreover, H atoms also become substitutional hydrogen ( $\text{H}_o$ ) by occupying substitutional oxygen sites.  $\text{H}_o$  also acts exclusively as donors in this configuration [15]. The hydrogen atoms which act as donors lead to the minimum amount of doubly charged and neutral impurity scattering, which is one of the reasons why the mobility could be so high. In Koida's report, it is stated that high mobility TCO could be achieved by sputtering an  $\text{In}_2\text{O}_3$  in an atmosphere dosed with water vapor. The water vapor functions as the hydrogen source in the experiment. One of the effects of introducing water vapor is formation of an amorphous layer rather than a polycrystalline structure. The solid phase polycrystalline structure will be obtained by post-deposition annealing process [16].

### **1.6. Objective**

Based on the background and the potential of IO:H, the main objective of this thesis is intended to develop high mobility IO:H TCO for thin film solar cell application. The

objective would be divided into smaller parts: understand the effect of processing condition on the film properties and test the application of TCO for thin film solar cells. The IO:H layer would be hoped to achieve sheet resistance that lower than  $10\Omega/\square$  with maintained mobility above  $100\text{ cm}^2/\text{Vs}$ .



## CHAPTER 2

### Physics, Synthesis, and Characterization of TCO

#### 2.1. Physics of TCO

Transparent conductive oxide layers have special properties which are high transparency in visible wavelength range and high electrical conductivity. Most of the TCOs materials are n-type semiconductors which mean defects such as oxygen vacancies, impurity substitutions and interstitial donate electrons to the conduction band by providing charge carriers for the flow of electric currents [17]. Research to optimize preparation of TCO thin film for large area deposition has been increase significantly. Some researches are discussing about low temperature processing of TCO for plastic substrate, improvement of uniformity of the TCO layer, higher deposition rate, etc. Among of these improvements, the resistivity of TCO films have saturated at about  $10^{-4} \Omega\text{cm}$  and would be able to reach  $10^{-5} \Omega\text{cm}$  under controlled laboratory conditions [17].

A good TCO should have low resistivity. From equation (1), in order to obtain very low resistivity, the mobility or the carrier density should be increased. However, there are several limitations that should be taken into consideration.

$$\frac{1}{\rho} = \mu n_e e \quad (1)$$

Where:  $\rho$  = Resistivity ( $\Omega \text{ cm}$ )  
 $\mu$  = Mobility ( $\text{cm}^2(\text{Vs})^{-1}$ )  
 $n_e$  = Carrier density ( $\text{cm}^{-3}$ )  
 $e$  = Electric charge ( $1.602 \times 10^{-19} \text{ C}$ )

The limitation of carrier density comes from its relation to plasma frequency. Plasma frequency is a natural frequency at which cloud of electron oscillates with respect to the fixed positive ions of the material. The oscillation of the electron cloud plays an important role in the optical properties of material. Photons that come to the TCO which have a lower frequency than the plasma frequency would be reflected by the electrons inside the material because they block the electric field of the photons. Equation (2) shows how to calculate the plasma frequency.

$$\omega_p^2 = \frac{\omega_N^2}{\epsilon_\infty} \quad (2)$$

Where:  $\omega_P$  = Plasma frequency (Hz)  
 $\omega_N$  = Unscreened Plasma Frequency (Hz)  
 $\epsilon_\infty$  = High Frequency dielectric constant

To obtain  $\omega_N$ , equation (3) should be used.

$$\omega_N^2 = \frac{n_e \times e^2}{m^* \times \epsilon_0} \quad (3)$$

Where:  $n_e$  = Carrier density ( $\text{cm}^{-3}$ )  
 $m^*$  = Effective mass of electron  
 $\epsilon_0$  = Free space dielectric constant

From these two equations, it could be concluded that if we increase the carrier density, the unscreened plasma frequency would be increased, which leads into higher plasma frequency. High plasma frequency will lead to more reflected light which has lower frequency. Hence there would be a tradeoff between the resistivity and the transparency [18]. Sharp step of reflection and transmission is showed in the vicinity of plasma edge. The steepness of the slope around the plasma frequency is determined by the mobility of the material. The higher the mobility, the steeper the plasma edge would be. Lower mobility would lead into increasing tail of the free carrier absorption, which reduce the transparency of the material [18].

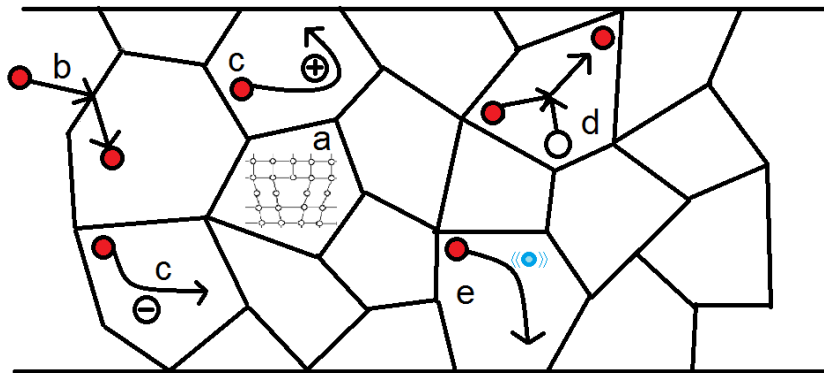


Figure 3. Scattering mechanisms in the TCO

There are several mechanisms that limit the mobility of carriers inside the TCO. Figure 3 shows several scattering mechanisms that might influence the mobility of carriers inside the TCO. The first mechanism is dislocation scattering which is shown in figure 3a. It is natural that a polycrystalline material has a lot of defects in forms of dislocation. However, dislocation scattering is not commonly used as mechanism to explain experimental data since it is difficult to obtain the value of the density of defects.

The second mechanism that limits the mobility of carriers is the scattering by grain boundaries. The scattering which is caused by grain boundaries is illustrated by figure 3b. Polycrystalline films have a lot of grain boundaries based on their mean grain size, which leads into crystallographically disturbed regions. Grain boundaries could create formation of defects in the band gap of semiconductors. Charge balance between the type of the carriers (electrons or holes) and types of the defects (electron trap or hole traps) causes either depletion or accumulation zones around the barrier. In TCO materials which are normally n-type materials, depletion zone are generated on both sides of grain boundaries accompanied with an energetic barrier with a height of  $\Phi_B$  for the electrons. The carrier transport in polycrystalline silicon was first described comprehensively by Seto. The assumption that he used for his experiment is a  $\delta$ -shaped density electron trap state in the band gap which completely filled. To illustrate the theory, figure 4 would be used.

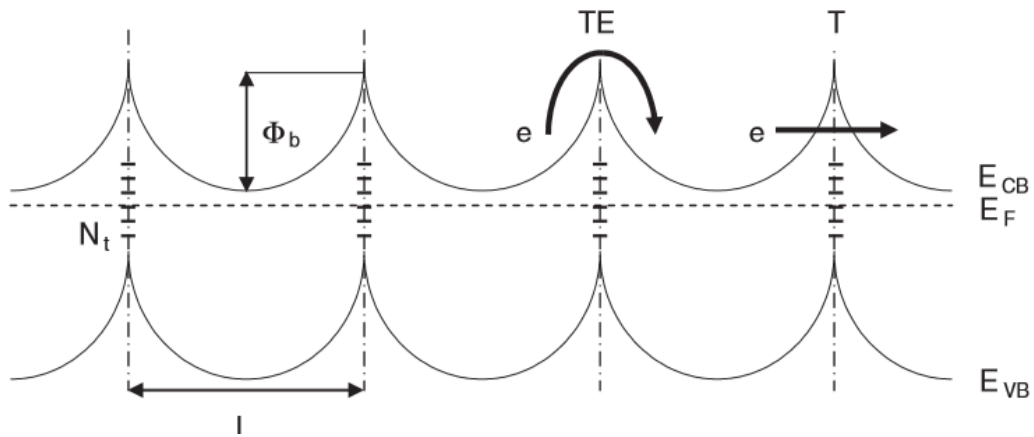


Figure 4. Schematic of charge transport at the grain boundaries [19]

Carrier transport mechanism across the grain barriers is displayed by the classical thermionic emissions depicted by path TE in figure 4. For a very high carrier concentration, the depletion width would be very narrow, which enables electrons to pass the barriers through quantum-mechanical tunneling.

The third mechanism that limits the mobility of electrons is ionized impurity scattering which is caused by screened coulomb potential of charged impurities (dopants) or defects. Scattering by ionized impurities is illustrated by figure 3c. The fourth mechanism is neutral impurity scattering which is caused by non-ionized impurities. The concentration of neutral donor in room temperature is very low which makes this scattering mechanism is negligible. The neutral impurity scattering is illustrated by figure 3d. The next mechanism that limits the mobility of carriers is optical phonon scattering. This

mechanism is caused by lattice vibrations of bonds in a polar semiconductor which induces an electric field that interact with a charge moving through the lattice. The phonon scattering is illustrated by figure 3e. Another mechanism is the acoustic-phonon scattering caused by an acoustic wave propagation through a crystal lattice which causes the atoms to oscillate about their equilibrium and interfere with the electron motion. The last mechanism is piezoelectric scattering which is caused by the electric field associated with lattice vibration in crystal where certain unit of cell does not contain a center of symmetry.[17][19]

Even though achieving low resistivity would need higher mobility and carrier density, in fact there is dependence between mobility and carrier density. This dependency is one of the limitation for achieving high mobility, since one of the scattering mechanism is ionized impurity scattering which comes from free carriers.[18]

**Table 1. Comparison between ITO, AZO, IO:H**

Properties	ITO (as-deposited / annealed)	AZO (as-deposited / annealed)	IO:H (as-deposited / annealed)
$R_s$ ( $\Omega/\square$ )	125 / 110	11.3 / -	28 / 35
$N_e$ ( $\times 10^{20} \text{ cm}^{-3}$ )	1.1 / 2.5	4.4 / -	3.55 / 1.38
$\mu_{\text{hall}}$ ( $\text{cm}^2/\text{V s}$ )	40 / 25	27 / -	50 / 115

## 2.2. Synthesis of IO:H

IOH layers were deposited by Radio Frequency (RF) sputtering at Else Kooi Laboratory TU delft. RF sputtering is one of the methods from physical vapor deposition. The other method that commonly used for sputtering is direct current (DC) sputtering and reactive sputtering. The difference between those sputtering methods is the power supplies that being used to generate the power. Compared to the other sputtering methods, one of the advantages of RF sputtering which has been compared to the other sputtering is the reduced trap density of the charge carrier by factor of 2.5. Lowering the trap density means that there will be a lower barrier height which can increase the mobility of electron [19]. The other advantage of using RF sputtering is there is no significant variation in plasma composition, because it could lead into inconsistent resistance [20]. The IO:H layers were deposited on  $10 \times 10 \text{ cm}^2$  corning glass. Before the deposition, corning glass was cleaned

by using fuming  $\text{HNO}_3$  (>99%) for 10 minutes and moved into boiling (>100 °C)  $\text{HNO}_3$  (69%) for another 10 minutes. The last step of the process was cleaning it with demineralized water. For the deposition,  $\text{In}_2\text{O}_3$  ceramic without dopant was used.

During the deposition, no external heating was introduced to the deposition chamber. The only component that leads to the increasing temperature was the sputtering itself. The argon that flows for every process was being kept at 40 sccm. The process pressure was being kept at  $5.7 \times 10^{-1}$  Pa while the base pressure was at  $1 \times 10^{-4}$  Pa. The target cleaning time was 600 s meanwhile, the rotation speed was 5 rpm. Some deposition parameters that become variables in this work are partial pressure of water, layer thickness, and deposition power. The deposition time was varied to adjust the layer thickness.

Some of the deposited layers would be annealed in vacuum oven. The purpose of the annealing is to increase the mobility of the layer. Both the annealing temperature and annealing time were varied. Figure 5 shows the sputtering setup that being used in this project.



**Figure 5. Sputtering setup for IO:H deposition**



## Chapter 3

### IO:H Development

#### 3.1. Basic Sputtering Process

##### 3.1.1. Effect of Power on Deposition Rate

In order to understand the effect of deposition characteristic on IO:H, the deposition power was varied. The deposition time was adjusted in order to keep the thickness of the sample to be at 100 nm.

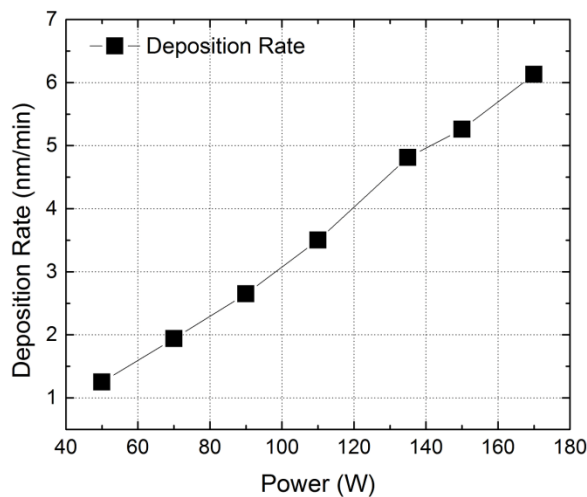


Figure 6. Deposition rate at different powers

The thickness of the deposited samples was measured by spectroscopy ellipsometry (SE). Therefore the deposition rate of the sample was estimated. From Figure 6 it could be seen that the deposition rate is linearly proportional to the deposition power. From the characterization result of the electrical properties of the samples which can be seen from appendix B, it seems that there was no major advantage to go into higher power. Knowing the fact that the mobility after annealing starts to decrease and the resistivity starts to increase after 150W, using higher power is not suggested.

Later on in this experiment, all of the deposition power that would be used is 135W. The value comes from the calculation in order to suit the other deposition machine in term of deposition power. The choice is also supported by the fact that in the range between 110W to 150W, there is no major difference in term of electrical properties.

##### 3.1.2. Effect of Partial Pressure of Water on Deposition Rate

According to Koida et al. (2007), water vapor plays an important role in order to obtain high mobility TCO. Thus, the deposition characterization should be observed before continuing to the TCO application.

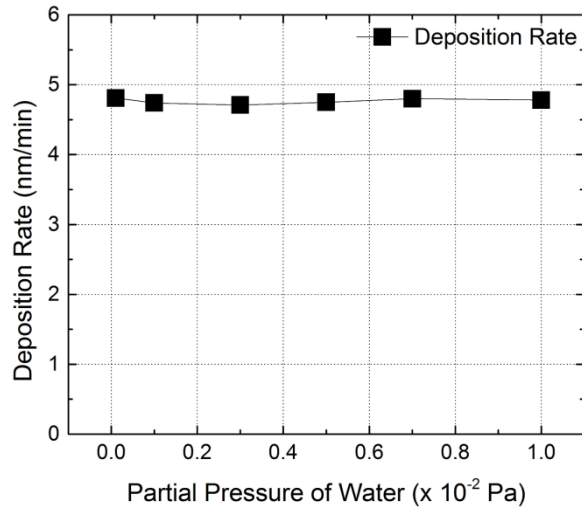


**Figure 7. Deposition rate for different partial pressure of water**

From figure 7 it could be seen that adding water vapor during deposition only gave a minor effect on the deposition rate. It means that to obtain the same thickness, the deposition time does not need to be changed. The effect of partial pressure of water in the IO:H layer would be discussed in the next section.

### 3.1.3. Uniformity of the Layer

One of the main problems that needs to be overcome in TCO development is the uniformity, especially on large area [21]. To check the uniformity of the layer, IO:H layer was deposited on corning glass which has been cleaned before. The glass that has been deposited with IO:H layer was divided into 9 pieces. The small piece of glass was characterized by SE to measure the thickness and afterwards it was cut into smaller piece. The IO:H layer on small piece of glass were to be characterized by hall measurement to check the electrical properties.

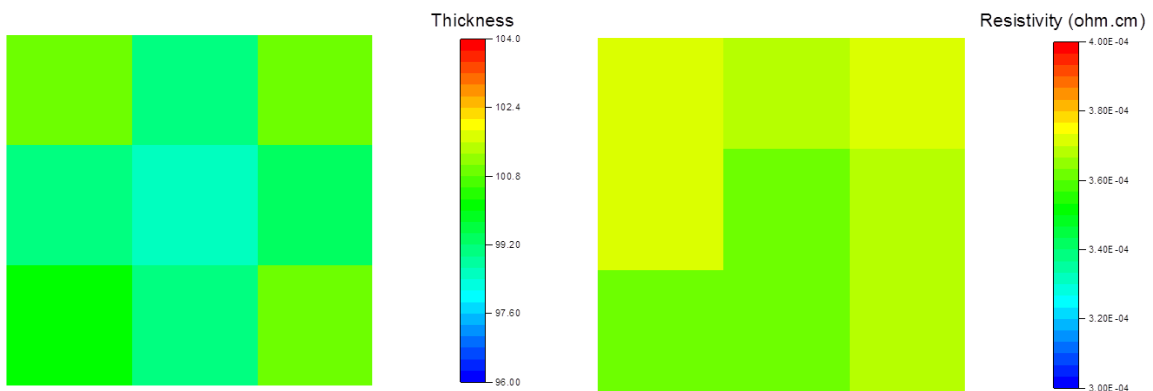


**Figure 8.a. Different thickness of the IO:H layer on top of 10 x 10 cm corning glass. b. Different resistivity of IO:H layer on top of 10 x 10 cm corning glass.**

From figure 8a it could be seen that the thickness of the layer is little bit thicker on the edge compared to the center of the glass. From the calculation, the average thickness of

the layer is 99.82 nm with standard deviation 1.07 nm. From the standard deviation value, the maximum difference on the layer thickness is 1.07% from the average thickness, which is magnificent. The electrical properties of the layer were checked to confirm the uniformity of the layer. From figure 8b it is shown that the resistivity of the layer is relatively uniform. From the calculation, it is obtained that the average resistivity through the layer is  $3.67 \times 10^{-4} \Omega\text{cm}$  with standard deviation of  $4.9 \times 10^{-6} \Omega\text{cm}$ . It is concluded that the ratio of the highest deviation and the average value of the sample is 1.34%.

### 3.2. Water Vapor Effect on IO:H layer

In order to understand the effect of water vapor in the development of the IO:H layer, sensitivity analysis should be done. The thickness of the sample was being kept at 100 nm. There were no external heat source introduced during the deposition and the only variable that varied between one sample and the other sample was the partial pressure of water. All of the samples were annealed with the vacuum oven for 30 minutes at 200 °C.

#### 3.2.1. Electrical Properties

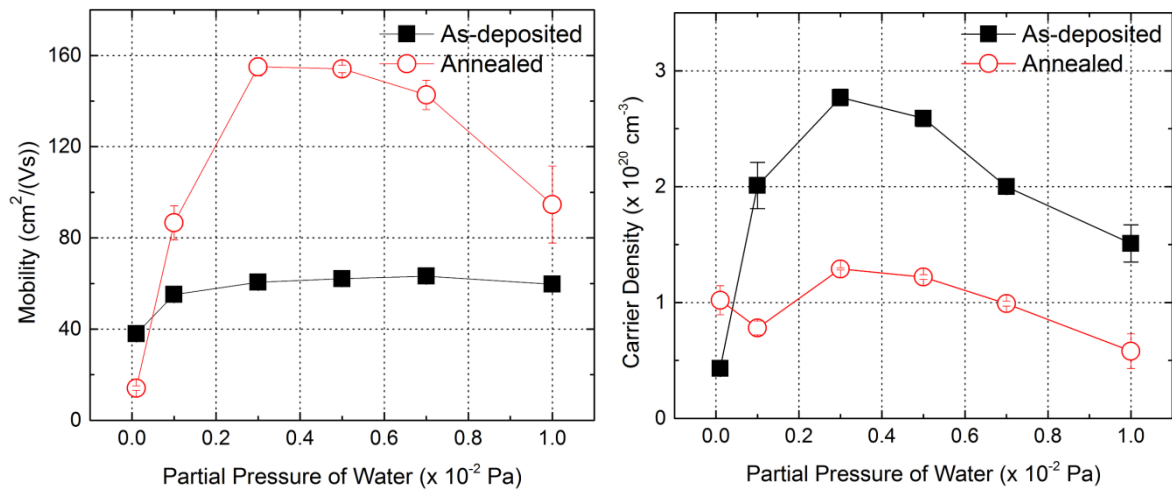
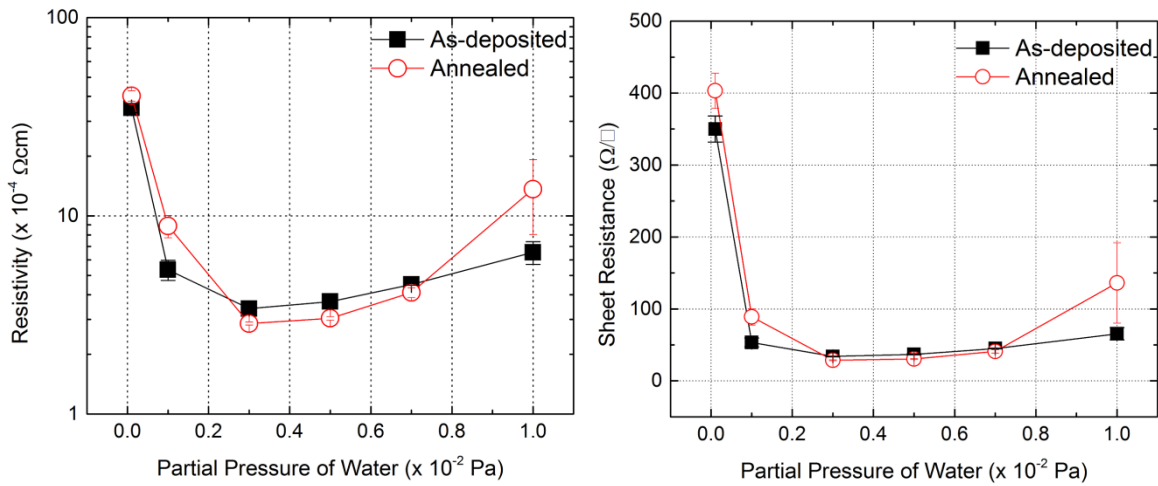


Figure 9.a. Mobility of IO:H layer with different partial pressure of water. b. Carrier density of IO:H layer with different partial pressure of water.

From figure 9a, the first data is the layer with no water vapor introduced during the deposition. However, it is very difficult to remove all of the water vapor from the wall of the deposition chamber, so it is assumed that the partial pressure of water for the first data is the base pressure which is  $1 \times 10^{-4}$  mbar. From figure 9a, the mobility from the as-deposited samples seems to be saturated at 60  $\text{cm}^2/(\text{Vs})$  and starts to decrease again with the increased partial pressure of water. After the annealing, the change of the sample mobility is divided into 3 scenarios. The first case is where mobility decreased after the annealing. This sample was the only one without external water vapor introduced. The second case

was where the mobility increased but insignificant. The third case was when the mobility increased significantly after the annealing. The highest mobility difference between as-deposited sample and annealed is obtained by the sample with partial pressure of water at  $3 \times 10^{-3}$  Pa during the deposition. The increase of the mobility of those samples reaches a factor of 2.6 and the mobility of the IO:H layer reaches 160 cm/Vs. It means that the mobility of IO:H layer after annealing has an optimum value. Figure 9b shows the carrier density of the layer. It could be seen that all of the carrier density drop by the factor of 2 after the annealing, except the layer which deposited with no water vapor introduced. The highest carrier density was obtained by the layer which deposited with the partial pressure of water at  $3 \times 10^{-3}$  mbar. It suits with the theory which said if the mobility increases, there is a tendency that the carrier density would decrease [19]. Both of the mobility and carrier density would give an effect to the resistivity as shown in figure 10.



**Figure 10.a. Resistivity of IO:H layer with different partial pressure of water. b. Sheet Resistance of IO:H layer with different partial pressure of water.**

It is obvious that the layer which deposited with  $3 \times 10^{-3}$  Pa partial pressure of water would have the lowest resistivity, since it has the highest mobility and the highest carrier density. The interesting thing in the resistivity is there are some differences in the change of resistivity after the annealing. The samples with no water vapor during the deposition, the resistivity increases even though the carrier density increases; this is caused by the increase in the carrier density. Another points show the increase in resistivity even though the mobility increases, this process could happen because of the compensation of increased mobility by reduced carrier density. The others samples show the resistivity become lower since the rise in mobility is higher compared to the drop in carrier density. Since all of the samples were kept with 100nm thickness, the calculation of the sheet resistance would be straight forward with equation (4).

$$R_s = \frac{\rho}{t} \quad (4)$$

Where :  $R_s$  = Sheet Resistance ( $\Omega/\square$ )  
 $\rho$  = Resistivity ( $\Omega\text{m}$ )  
 $t$  = Thickness (m)

It is clear that the role of water vapor during deposition is very important; since the sample without water vapor introduced during the deposition has a very high resistivity, low mobility and carrier density. The water vapor acts as a hydrogen supplier in the IO:H layer. The hydrogen would form a shallow donor state in metal oxide [15]. From RBS result of Koida et al. the increasing partial pressure of water would lead into a drop in In and O composition in IO:H layer, and an increase in H composition. From the same work, it is reported that after the annealing, there is only minor change in the composition for In, O and H in the layer [22].

It has been predicted by Nakazawa et al (2006) that indium oxide would have three regions of electrical properties. The study from Nakazawa shows the region of the carrier density is between  $10^{18}\text{cm}^{-3}$  and  $10^{21}\text{cm}^{-3}$ . The first region is  $\text{In}_2\text{O}_3$  layer with high carrier density ( $>10^{20}\text{cm}^{-3}$ ) and very high mobility ( $>100\text{cm}^2/\text{Vs}$ ).  $\text{In}_2\text{O}_3$  in this region there is a very small amount of structural defects. The screening effect is strong and the carriers are not localized around the oxygen vacancies, which could lead the phonon scattering become the most dominant properties that able to limit the mobility. The second region is the material with high carrier density, which typically has the same carrier density as the first region, but has lower mobility ( $30\text{cm}^2/\text{Vs} < \mu < 100\text{cm}^2/\text{Vs}$ ). These materials normally have a lot of structural defects, which makes the most dominant scattering mechanism are the ionized impurities scattering. The ionized impurity scattering would be in the form of oxygen vacancies. The third region would be the low carrier density and low mobility area. This material typically has a lot of structural defects, and the low carrier concentration leads into a tendency of the carriers to be localized. The localization would be helped by structural defects which offer some localization sites. In this region, the phonon scattering becomes less important, and the factor that decrease the mobility is the localization [23].

From the previous work  $\text{In}_2\text{O}_3$  with mobility above  $100\text{cm}^2/\text{Vs}$ , would have a carrier density below  $10^{18}\text{cm}^{-3}$ . It was reported by Weiher (1962) that  $\text{In}_2\text{O}_3$  was able to obtain hall mobility of  $160\text{cm}^2/\text{Vs}$  and with a carrier concentration of  $3.5 \times 10^{17}\text{cm}^{-3}$ [24]. Further research by Galazka et al. which shows  $\text{In}_2\text{O}_3$  could reach mobility of  $180\text{cm}^2/\text{Vs}$

with a carrier concentration of  $1.2 \times 10^{17} \text{ cm}^{-3}$  [25]. The increase in the carrier density of the sample with no water vapor introduced during deposition has been predicted by Galazka in his work. Indium Oxide crystal would increase the carrier density by the factor of 2 with temperature treatment at  $200^\circ\text{C}$ , and it would reach a maximum carrier concentration with temperature of  $700^\circ\text{C}$  [25].

### **3.2.2. XRD Characterization**

To get a better understanding about the properties of the IO:H layers, XRD characterization has been done to analyze the layers.

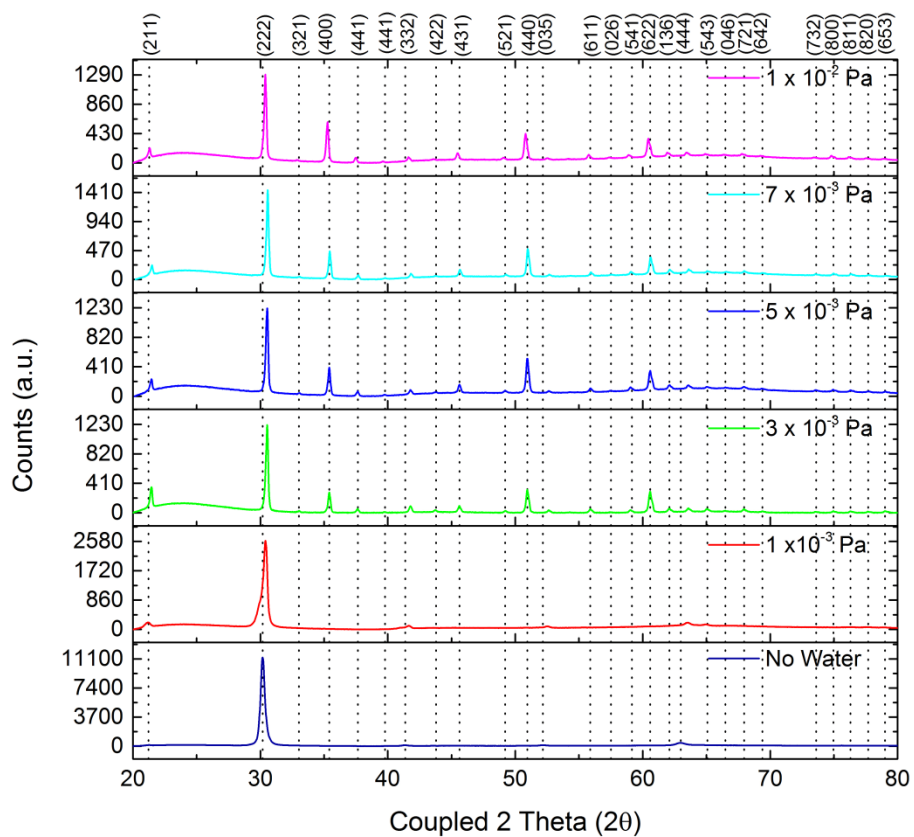
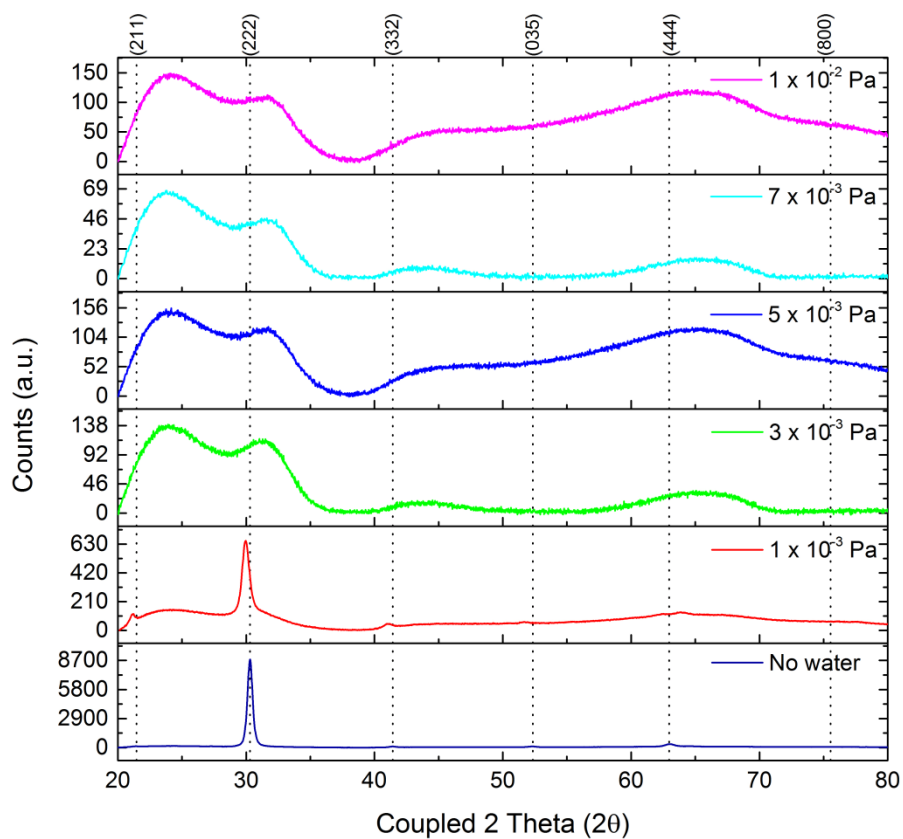


Figure 11.a. XRD results for as-deposited IO:H layers with different partial pressure of water. b. XRD results for annealed IO:H layers with different partial pressure of water.

Figure 11a shows the XRD characterization of the as-deposited samples, and figure 11b shows the XRD characterization of annealed samples. XRD result from top to bottom is IO:H layer which deposited without water vapor, and the water vapor increases gradually as going down in the figure 11. From the as-deposited result, it could be seen that the layer without water vapor during the deposition have a polycrystalline phase. When water the vapor was introduced, the layer turned out to be mixed phase between polycrystalline and amorphous structure. By adding more water vapor during deposition the sample would be turned into amorphous phase. It was stated by Koida in his work that the water vapor suppresses the crystal growth of the material thus the IO:H becomes amorphous [16]. The reason why the water vapor suppresses the growth of the crystal is due to the adhesion of H atoms, OH, or H<sub>2</sub>O molecules [26]. After the annealing, all of the samples turned into polycrystalline, but the layers which are deposited as amorphous phase have random crystal orientation compared to the layers which deposited as crystalline. With Scherrer's equation, the crystallite size of the layer could be calculated. For this calculation, it is assumed that for all of the polycrystalline samples were completely crystallized.

$$\tau = \frac{K \lambda}{\beta \cos \theta} \quad (5)$$

Where:  $\tau$  = Mean crystallite dimension (nm)  
 $K$  = dimensionless factor (0.94)  
 $\beta$  = Full Width Half Maximum (rad)  
 $\theta$  = Bragg Angle (°)

The result of the mean crystallite size calculation for orientation  $d_{222}$  was shown in table 2.

**Table 2. Result of XRD calculation**

Partial Pressure of Water (Pa)	Peak position [222] (2θ)	FWHM (2θ)	Particle Size (nm)
<b>As-deposited</b>			
$1.00 \times 10^{-4}$	30.29	0.4610	20.84
$1.00 \times 10^{-3}$	29.85	0.7852	12.18
<b>Annealed</b>			
$1.00 \times 10^{-4}$	30.19	0.3922	24.47
$1.00 \times 10^{-3}$	30.40	0.4014	23.91
$3.00 \times 10^{-3}$	30.53	0.2208	43.62
$5.00 \times 10^{-3}$	30.55	0.2247	42.87
$7.00 \times 10^{-3}$	30.57	0.2118	45.48
$1.00 \times 10^{-2}$	30.40	0.2156	44.62

From Table 2, it is clear that the crystal growth of the IO:H layer was polycrystalline originally, therefore introducing water vapor will suppress the growth of the layer lead to smaller crystallite size. It can be seen from the data of as-deposited sample. In the Scherrer's equation, all of the crystals were assumed as a sphere, but in reality, the shape of the crystals might be different. Therefore in this report, the crystallite size defines as a length of a group of crystal with the same crystal orientation. This statement is to emphasize that the crystallite size is different with particle size and not always the same as grain size [27]. Smaller crystallite size with the increase of water vapor could have a meaning that during the deposition, the water vapor tends to change the orientation of the crystal growth. The smaller grain size could be the result of creation of In-OH bonding instead of In-O-In, which makes the chain shorter. One clear example could be seen from comparing the crystallite size of as-deposited sample without water vapor and the sample with  $1 \times 10^{-3}$  Pa water vapor partial pressure. The water vapor makes the crystal structure unorganized which causes the crystallite size becomes smaller. Furthermore, higher partial pressure of water vapor creates a mess during the deposition and makes the layer becomes amorphous. Annealing leads into the increase of the crystallite size of the sample with no water vapor during the deposition. Besides, it also increases the crystallite size for the sample with lowest partial pressure of water. The interesting fact is the crystallite size of annealed sample which is deposited in amorphous phase has the largest crystallite size compared to the sample which is deposited as polycrystalline. In term of crystallinity, the sample which deposited as polycrystalline has single dominant orientation; while sample which deposited as amorphous and then annealed would have a random orientation.

If we relate the XRD result with the electrical properties of the layer, there is a correlation between both of the data. First correlation is about the carrier density, for all of the samples which are deposited as amorphous phase and then crystallized by annealing, they would have a drop in carrier density by a factor of 2. This includes the sample with mixed phase of crystal and amorphous. During the annealing, external energy was introduced to the system which leads the crystal to rearrange itself. The rearrangement of the crystal leads into the reduction of number of defects. From work of Koida et al in 2010, it is stated that in the amorphous phase, the doubly charged impurities in the form of oxygen vacancies was limiting the mobility [28]. During the crystallization the H<sub>2</sub>O molecules inside the layer are desorbed, and the H and OH inside the grain migrate towards the grain boundaries. Koida proposed that the structural arrangement during crystallization eliminate oxygen vacancy and generate H<sup>+</sup> add a singly charged donor. Assuming that all of the charge from the amorphous phase comes from the oxygen vacancy which have two free electron, and all of them was substituted by singly charged donor which have one free electron, then it might be the reason why the carrier density drops by a factor of two after annealing [28].

Others scattering mechanisms that affect the mobility in TCO materials besides impurity scattering are phonon scattering, grain boundary scattering, neutral impurity scattering, and etc. From the work of Macco et al, it is known that neutral impurity scattering are negligible, even though the amount of hydrogen atoms that become an active dopants inside the layer is around 4%. After the annealing, there are only two main scattering mechanisms existing, which are the singly charged impurities and phonon scattering [29]. The phonon scattering also plays an important role in limiting mobility, but phonon scattering could not be avoided and would always appear in both as deposited film and annealed film [29]. The grain boundary seems to be unimportant in limiting mobility since the observed optical mobility and hall mobility have the quite similar value. However, Wardenga et al propose that the low effect of grain boundaries in the mobility is related to the passivation effect of H after crystallization process. During the annealing, In(OH)<sub>3</sub> decomposes, and the hydrogen saturates the grain boundary which leads into lower the effective trap densities. By lowering the trap densities, the potential barriers at grain boundaries decreased [30]. The theory suggested by Wardenga is different from the other theory, since the others report that high mobility is obtained by the improvement of intra-grain properties due to crystallization process [7].

### 3.2.3. Raman Spectroscopy Characterization

To understand the crystal structure of the layer, Raman spectroscopy characterization needs to be done. Raman Characterization had been done by Valeria Russo in Politecnico di Milano.

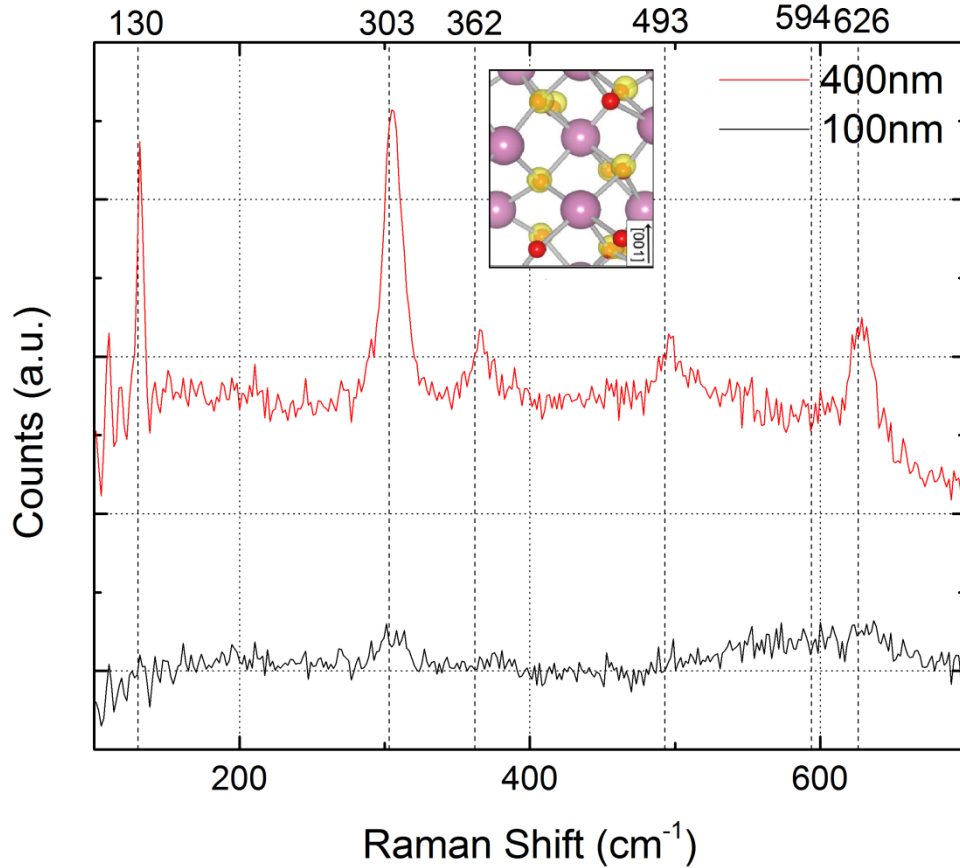


Figure 12. Raman setup for annealed IO:H layer with 100nm and 400nm thickness. Inset : BCC structure of defect free In<sub>2</sub>O<sub>3</sub> crystal [31]

Both of the samples have the principle peak of In<sub>2</sub>O<sub>3</sub> that agrees with the work of Chong et al [32]. Both of the samples are the annealed sample since the as-deposited samples shows no signal during the measurement. One interesting thing is by introducing water vapor during the deposition the measurement signal seems to be stronger. The observed Raman peaks correspond to the phonon vibration modes of the BCC In<sub>2</sub>O<sub>3</sub>. This finding is agree with the work of Reunchan et al. which report that the structure of IO:H would be BCC [31].

### 3.2.4. Optical Properties

One of the most important factor to decide whether a TCO is good for solar cell application or not is the optical properties of the TCO itself. A good TCO would ve expected to have a high transparence and low absorption. It is also important to understand

the refractive index ( $n$ ) of the TCO. Non-suitable  $n$  of the TCO and the absorber layer could lead into reflection in top side of TCO which leads into lower efficiency of solar cell.

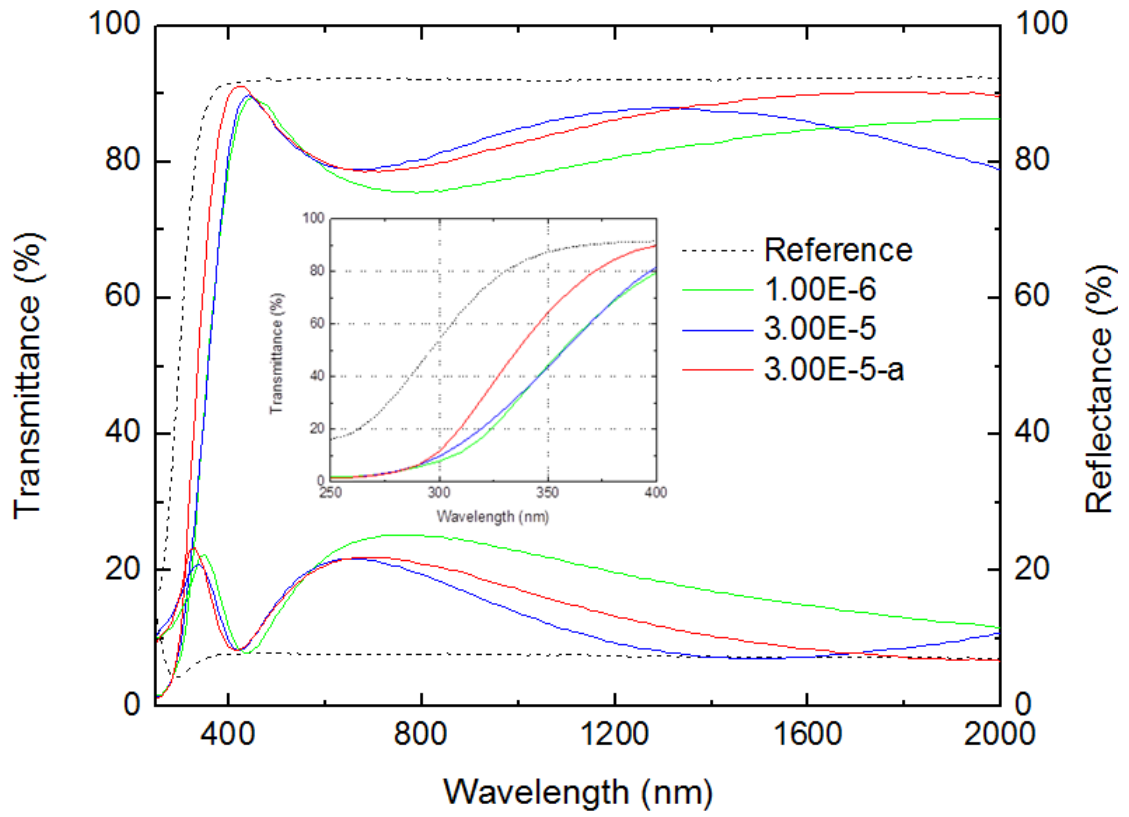
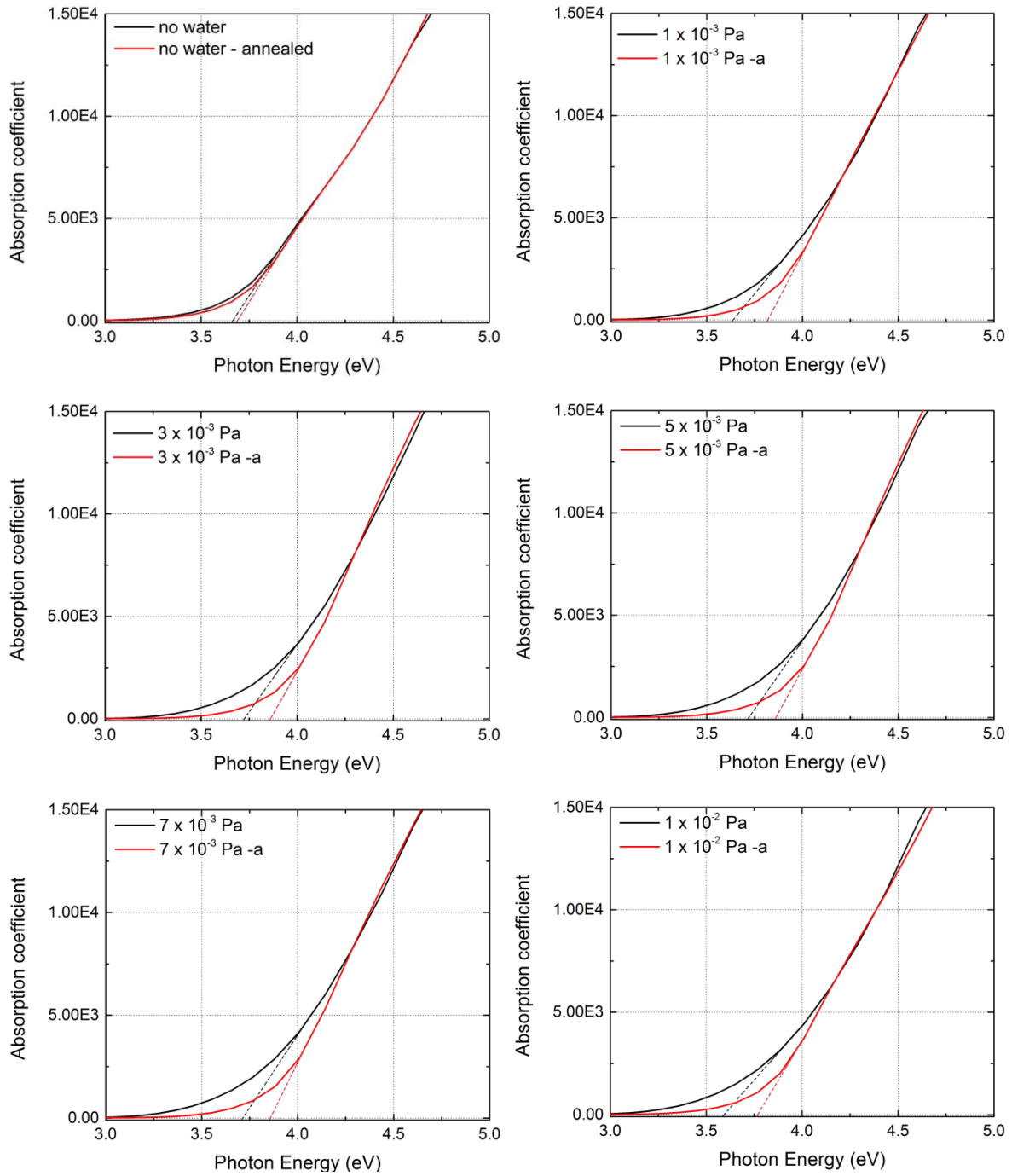


Figure 13. Transmittance and Reflectance of IO:H layer. Inset : Transmittance between 250nm-400nm.



**Figure 14. Absorption coefficient of IO:H layer with different partial pressure of water**

Figure 13 shows the transmittance and reflectance of the IO:H layer. The reference in figure 13 is the glass that being used in this work. In the short wavelength region near the band edge, the annealed IO:H sample has steeper increase. While in the visible region, all of the TCO have comparable transparenance and reflectance, except in the red spectrum region where the sample with no water vapor during deposition becomes more reflective and less transparent. By increasing partial pressure of water during, the sample turned out

to be less reflective. It might be caused by the difference in the n value of the samples. Figure 14 shows the absorption coefficient of the IO:H layer.

**Table 3. Calculation result of Bandgap and value of n at wavelength 598nm and 1000nm**

Partial Pressure of water	$\lambda_{\text{gap}}$	Bandgap (eV)	n (at 598nm)	n (at 1000nm)
<b>as deposited</b>				
<b>1.00E-06</b>	352	3.52	2.0995	2.029
<b>1.00E-05</b>	347	3.57	2.026	1.8573
<b>3.00E-05</b>	337	3.68	2.0111	1.7797
<b>5.00E-05</b>	339	3.66	2.021	1.8087
<b>7.00E-05</b>	346	3.58	2.0366	1.8452
<b>1.00E-04</b>	351	3.53	2.049	1.8697
<b>annealed</b>				
<b>1.00E-06</b>	348	3.56	2.0811	2.0091
<b>1.00E-05</b>	325	3.81	2.0329	1.9218
<b>3.00E-05</b>	320	3.88	2.0057	1.8689
<b>5.00E-05</b>	321	3.86	2.0179	1.894
<b>7.00E-05</b>	324	3.83	2.0203	1.9071
<b>1.00E-04</b>	330	3.76	2.0228	1.9171

From the calculation, it is known that the band gap of the IO:H layers changes by introducing water vapor during the deposition, and it would further increase after the annealing process. The difference between the samples with the band gap is the tail state. One reason that could explain the difference in the tail state condition is the reduced amount of defect inside the IO:H layer, it is because the sample with no water vapor introduced during deposition has a very low mobility. Since the mobility has a relation with the trap density, it could be assumed that lower mobility might be caused by a higher amount of defects. However, the result would not fit the Burstein-moss effect. The Burstein-moss effect states that higher carrier density would increase the absorption edges towards higher energy level [33]. But in the developed IO:H layer that is not the case, the IO:H layer with no water vapor introduced during the deposition would have lower optical band gap compared to sample with partial pressure of  $3 \times 10^{-3}$  Pa. The annealed samples have a higher optical band gap compared to the as-deposited samples, even though the carrier density of the sample drops by the factor of 2 after the annealing. The reason behind this phenomena might be the disorder structure inside an amorphous structure of the as-deposited IO:H layer which forbid the optical transition [30].

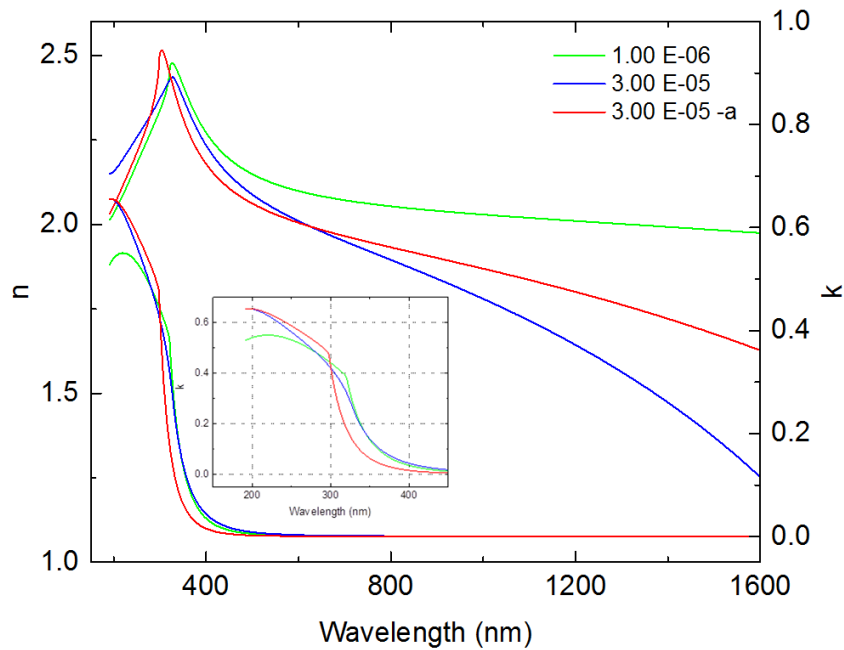


Figure 15. Result of  $n$  and  $k$  from IO:H layer. Insert :  $k$  value for wavelength 200nm to 450nm

From the work of Fujiwara and Kondo, it is stated that by increasing the carrier concentration, the  $n$  value would decrease, especially in the higher wavelength due to the Burstein-Moss effect. The carrier concentration of the IO:H layer affects the broadening effect of the peak in the  $n$  value. Width parameter of the peak is inversely proportional to the lifetime of the carriers or excitons. It could lead into a meaning that the broadening of the peak reduces the lifetime of excitons inside the layer, which also implies that the increasing of carrier concentration would reduce the lifetime of the excitons. This effect could be caused by the screening of coulomb potential. The Coulomb attraction in an electron hole pair concentration is screened by free electron surrounding the exciton, resulting in reduction the stability of the exciton [33].

### 3.2.5. Positron Annihilation Spectroscopy

One of the most advanced technology to understand the mechanism that happens inside a material is photon annihilation spectroscopy (PAS). It could be applied to understand the defect inside a material especially for charged defects like oxygen or indium vacancies.

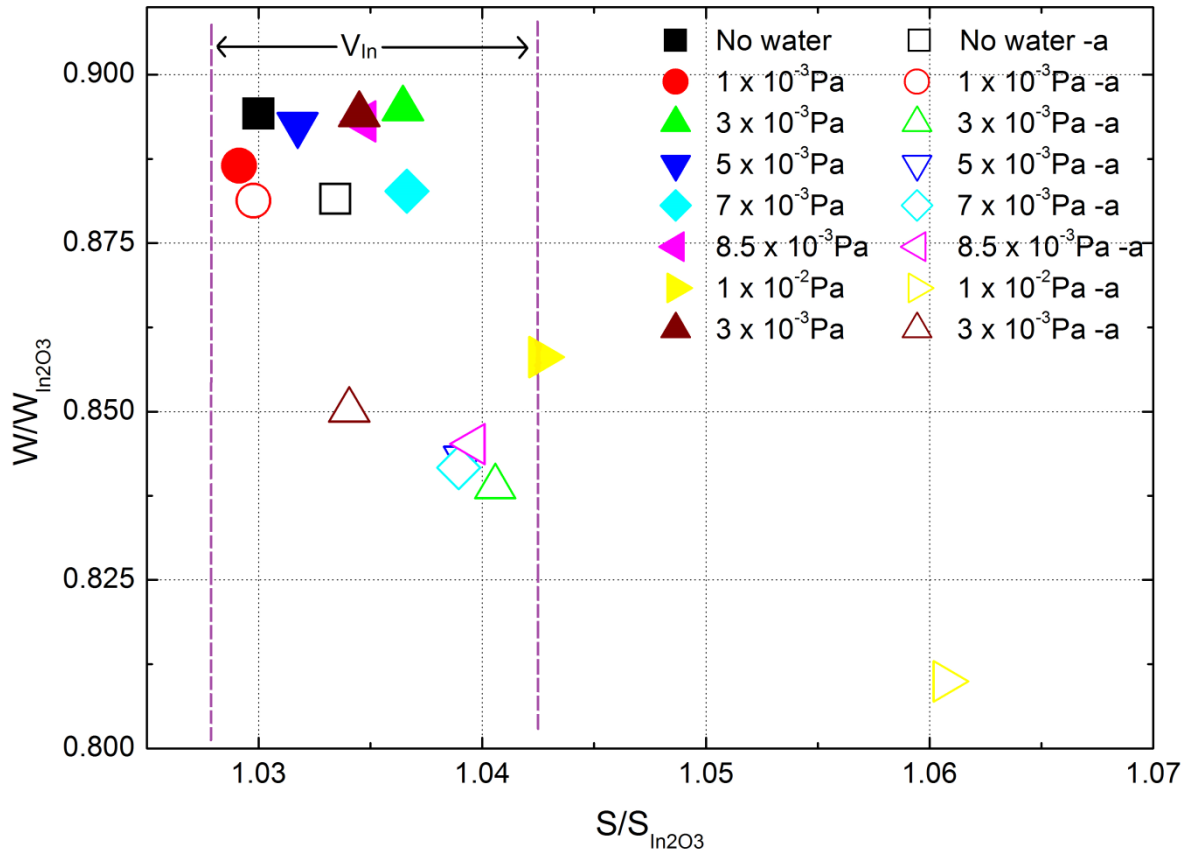
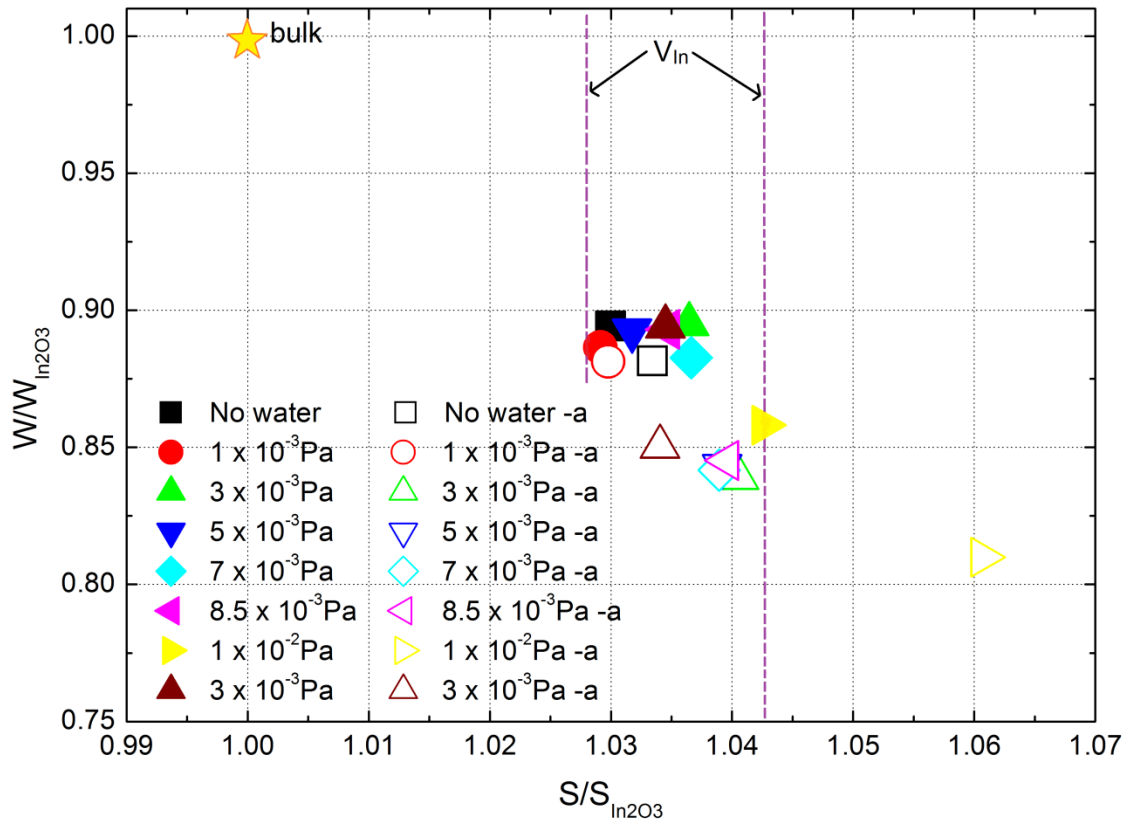


Figure 16.a. Normalized developed IO:H layer with Bulk  $\text{In}_2\text{O}_3$  crystal. b. Normalized IO:H layer zoomed in

Figure 16a shows the result of PAS characterization of the IO:H layers. In general, by introducing water vapor during the deposition, the S-parameter would increase into higher value. The S-parameter reflects the valence electron of the sample. If the positron annihilate a slow moving electron, it will resulting a narrow annihilation peak. Higher S-parameter value related to increasing partial pressure of water indicates that there are more defects, or bigger free space area in the material which formed from interaction between indium vacancies and oxygen vacancies. While W parameter shows the wing parameter of doppler broadening result, it correlate with S-Parameter since the absolute value will be similar. It proposes a meaning that higher S will lead into lower W. Indium vacancy ( $V_{In}$ ) point in the figure 16a obtained from simulation work of Makkonen et al. from aalto University Finland [34].

Introduction of defects would lead into higher S value and lower W value in the PAS characterization. It is shown in the IO:H layer which has been developed in this project,  $V_{In}$  might be one factor which limit the mobility. However, the last point of the measurement, the IO:H layer with partial pressure of water vapor of  $1 \times 10^{-2}$  Pa has completely different S-W value compared to the other IO:H layers. This might be the clustering of  $V_{In}$  and  $V_O$  inside the layer which creates bigger open volume inside the material as-stated by Reurings et al [35]. It was stated in the similar report that the  $V_O$  solely will not trap the positron. The vacuum annealing might migrate the  $V_O$  in the layer to cluster with  $V_{In}$  and, it might be done during the crystallization process. The clustering of  $V_{In}$  and  $V_O$  would reduce the charge of  $V_O$  which becomes less effective to act as an electron trap. The effect of water vapor during the deposition might be the source of hydrogen, which passivates the  $V_O$  inside the layers [36]. It could be seen in figure 16b the developed IO:H layers seems to be clustered in one place. It might be the result of passivation of hydrogen in the layers which reduce the effect of  $V_O$  in vacancy cluster and leave  $V_{In}$  in the cluster.

### 3.3. Effect of Annealing Temperature

In order to apply the developed IO:H on thin film solar cells, an understanding about temperature dependence of IO:H is really important. It is because the processing of each type of thin film solar cells is completely different. Starting with the substrate and superstrate configuration of solar cells, and then continued by deposition of the absorber layer which might use specific temperature that has been optimized before. For this experiment, the layer was kept at 100 nm thickness and the time for the annealing was being kept at 30 minutes.

#### 3.3.1. Electrical Properties

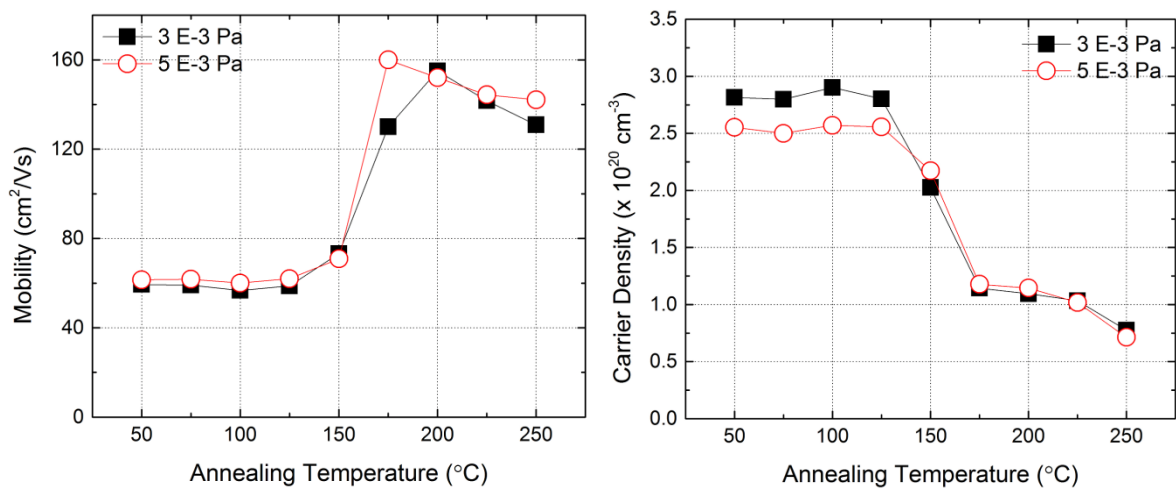
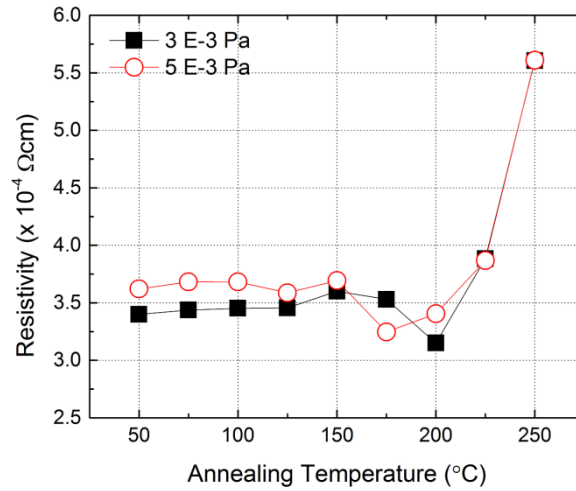


Figure 17.a. Mobility and b. carrier density of IO:H layer with different annealing temperature

Figure 17 shows the mobility and carrier density of IO:H layers, which have been treated with different annealing temperature. From both of the result, it points out that the electrical properties of the sample experienced a change at annealing temperature 150 °C. However it has been reported by Macco et al., that by annealing temperature of 150 °C, the annealing time to reach crystallinity of 100% was more than 100 minutes [29]. However, the significant difference from the as-deposited sample was obtained with annealing temperature of 175 °C. Moreover, the optimum mobility of both samples was obtained from different annealing temperature. Sample which deposited with partial pressure of water vapor 3.00 x 10<sup>-3</sup> Pa has temperature of annealing of 200 °C, while sample which deposited with water vapor of 5.00 x 10<sup>-3</sup> mbar has optimum temperature of 175 °C.



**Figure 18. Resistivity of IO:H layer with different annealing temperature**

The resistivity of the IO:H layer remains constant before the annealing temperature at 150 °C. Different resistivity drop is experienced by both of the samples. The lowest resistivity of the sample was obtained where the sample has highest mobility, since the sample did not experience significant change in of carrier density for annealing temperature at 175 °C and 200 °C.

### 3.3.2. XRD Characterization

Figure 19 indicates that the temperature annealing of 175 °C for 30 minutes, could make the sample fully crystallized. If the XRD result is being correlated with the electrical properties of the IO:H layers, the sample would have better properties when the sample was already crystallized. This result shows that the solid phase crystallization by annealing has a very important role to achieve a better properties of IO:H layers. But, there is an interesting fact related to the annealing, in macco et al. work, it was reported that the properties of the IO:H layer was related to crystallinity of the layer [29]. The annealing temperature doesn't play an important role in the electrical properties. After all this work shows that that higher annealing temperature can make the layer becomes more resistive.

**Table 4. Calculation of IO:H for different annealing temperature**

Annealing Temperature (°C)	FWHM (2θ)	Peak Position (2θ)	Particle Size (nm)
175	0.1977	30.69	48.81
200	0.1803	30.69	50.27
225	0.1808	30.69	53.37
250	0.1805	30.67	53.45
300	0.186	30.69	51.88

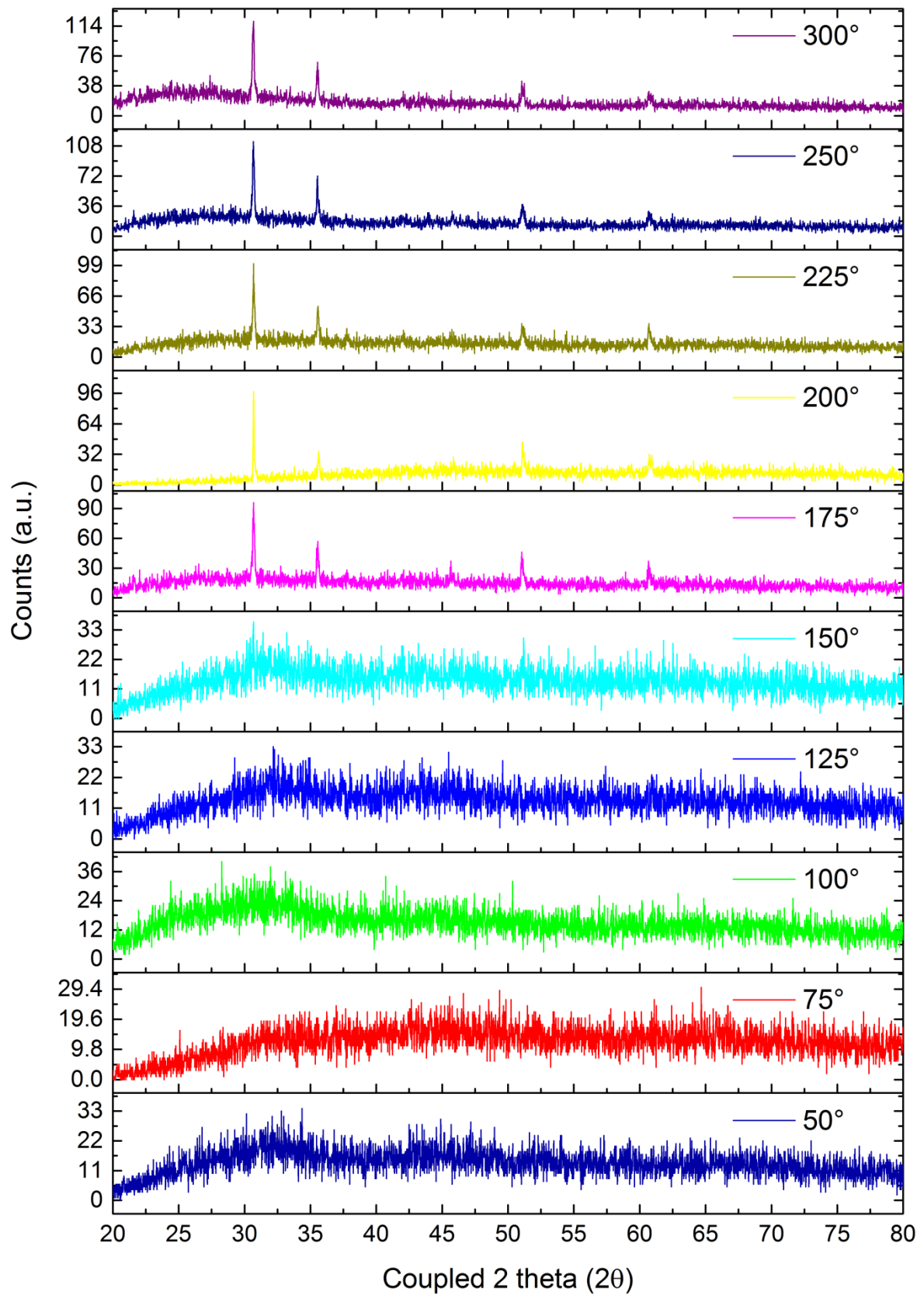


Figure 19. XRD characterization of IO:H layer with different annealing temperature

### 3.4. Thickness Effect on IO:H Layer

In order to obtain low sheet resistance, it is common to increase the thickness of the TCO layer, especially in the case of ZnO. It is because in ZnO, the resistivity remains constant at certain point, which makes the sheet resistance drop when the thickness is increased. In order to understand the resistivity of the IO:H layer for different thickness, the mobility and carrier density would be observed. To isolate the effect of thickness, all of the parameters during the deposition were kept constant. The partial pressure of water that being used during deposition was be  $3 \times 10^{-5}$  mbar.

#### 3.3.1. Electrical Properties

The electrical properties of the layer with different thickness were measured.

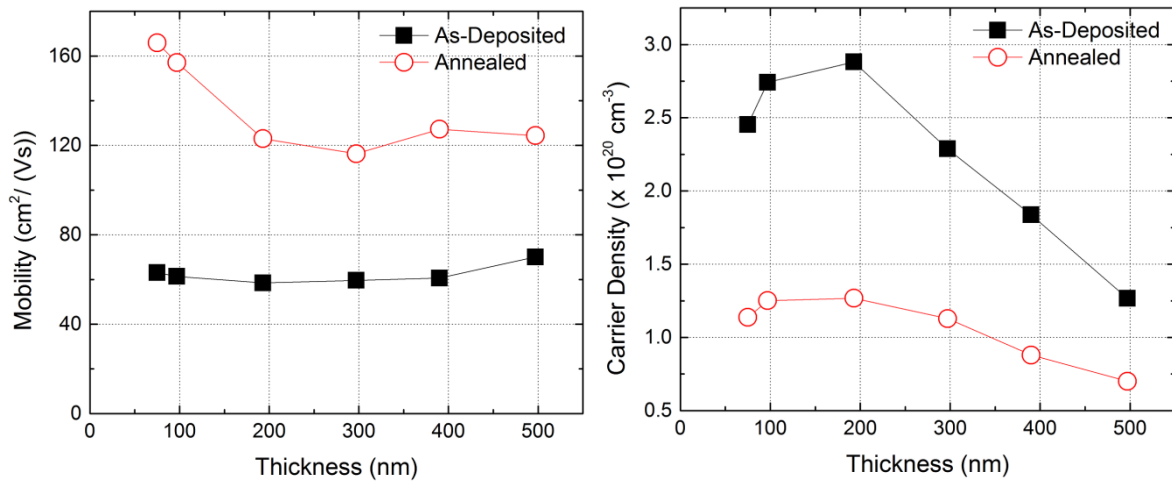
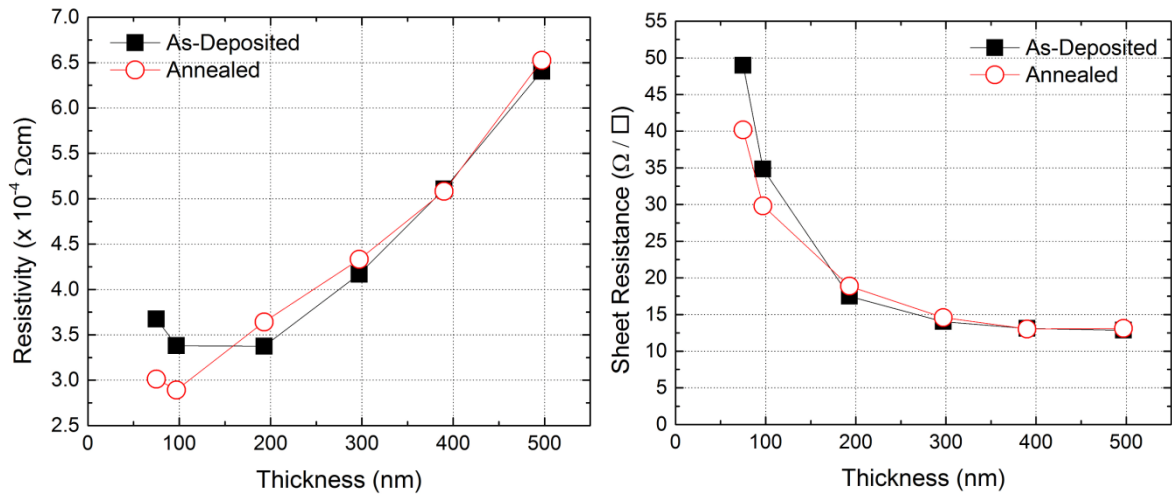


Figure 20.a. Mobility and b. Carrier density of IO:H layer for different thickness

Figure 20 indicates that the mobility of the as-deposited samples is almost flat around  $60 \text{ cm}^2/\text{Vs}$ . But after the annealing, the samples would perform two different characteristics. First characteristic was the annealed samples could reach mobility above  $150 \text{ cm}^2/\text{Vs}$ . And the second characteristic was when the mobility of the samples is seemed to be limited at  $120 \text{ cm}^2/\text{Vs}$ . The carrier density of the IO:H layer increased until 200 nm thickness, and after that, it decreased. After the annealing, all of the carrier density dropped. The interesting fact is the drop of the carrier density did not fall by the same factor as the samples in the partial pressure of water series. The drop of the carrier density was increasing until 200nm and then decreased on the thicker layer. The combination of mobility and the carrier density of the layer would result a resistivity in figure 21.



**Figure 21.a. Resistivity and b. Sheet resistance of IO:H layer for different thickness**

The resistivity of the layers increases linearly while the thickness of the layer increases. However, the resistivity of the as-deposited layers with 100 nm and 200 nm thickness have similar resistivity, which means that the sample with 200 nm thickness has the most benefit by increasing thickness since the resistivity of the sample starts to increase after 200 nm. It could be seen in the figure 21 that shows the sheet resistance of the sample. The sheet resistance shows that the lowest drop is between the as-deposited samples with 100 nm and 200 nm thickness of IO:H. Carrier density drop was the main cause in the increasing resistivity since the mobility of the sample remain constant with increasing thickness. Nonetheless, the sample has different behavior after the annealing. The sample with thickness of 75 nm and 100 nm would get benefit from annealing. It has the same reason with the series of partial pressure of water. The increase in mobility outweighs the drop in the carrier density. The drop in the sheet resistance with increasing the thickness has been predicted before, but it seems that the sheet resistance has reached its minimum point and could not be reduced further, even with increasing thickness.

### 3.3.2. XRD Characterization

To understand the effect of thickness in the layer, XRD characterization has been done.

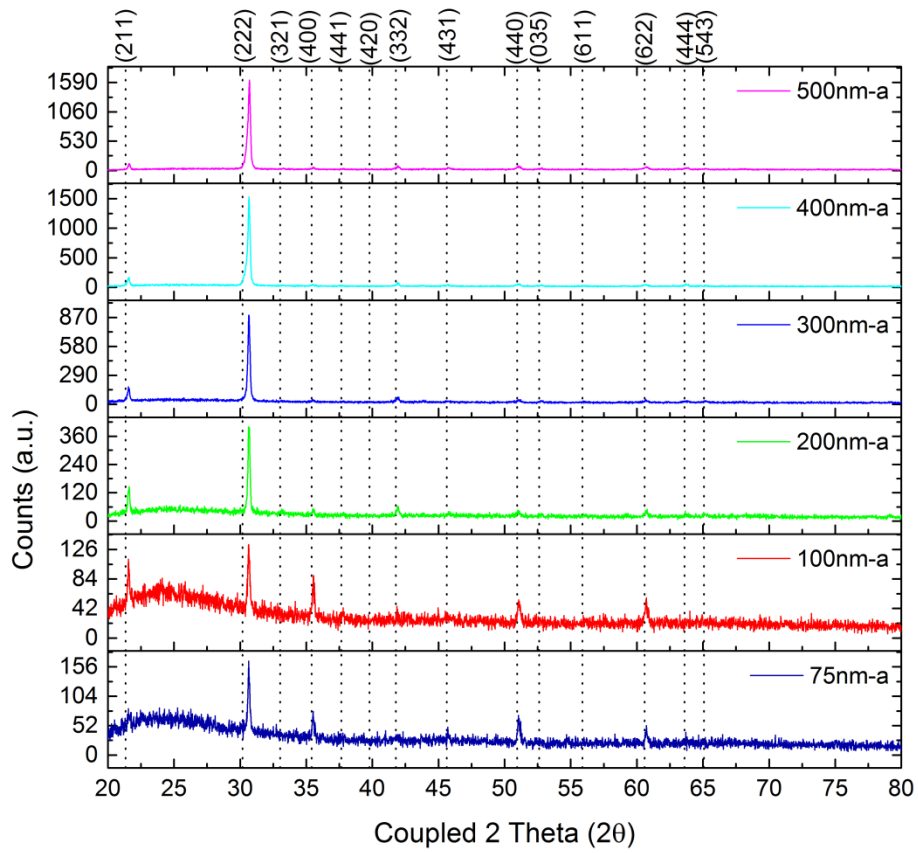
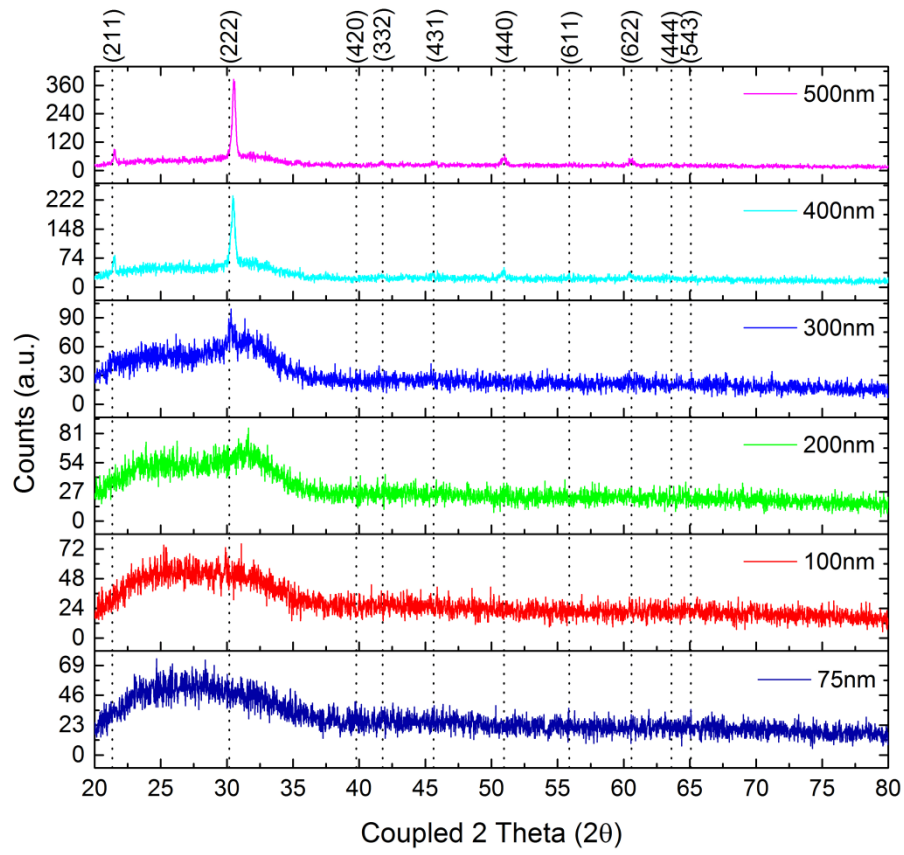


Figure 22. XRD characterization for sample with different thickness a. as-deposited and b. annealed

It could be seen from figure 22a, the layer turns out to be crystallized in the as-deposited sample after certain thickness. The reason why after certain thickness the samples was turned to crystallize is at the beginning of the deposition, the substrate was deposited in amorphous phase, but after certain thickness, crystallites nucleate at the surface. These crystallites would grow in size and new crystallites nucleate at thicker layer [37]. From the post annealing result showed in figure 22b and it shows that the orientation between the samples that has crystallized during the deposition showed less random orientation, compared to samples which deposited in amorphous phase. It is similar with the XRD result from IO:H layer with different partial pressure of water result. Afterwards equation 5 was used to calculate the particle size of the sample.

**Table 5. XRD calculation for IO:H layer with different thickness**

Thickness	Peak Position (2 $\theta$ )	FWHM (2 $\theta$ )	Particle Size (nm)
<b>as-deposited</b>			
<b>400</b>	30.45	0.4192	22.96
<b>500</b>	30.51	0.3122	30.85
<b>annealed</b>			
<b>75</b>	30.65	0.285	33.84
<b>100</b>	30.65	0.2424	39.78
<b>200</b>	30.63	0.1951	49.42
<b>300</b>	30.67	0.2038	47.32
<b>400</b>	30.67	0.1996	48.34
<b>500</b>	30.71	0.2327	41.47

From the calculation of the crystallite size, it seems that by increasing the thickness of the as-deposited layer; the particle size becomes bigger. It might be the result of longer chain of In-O-In which leads into longer crystal. After the annealing, all of the samples would be crystallized and all of them have a bigger particle size compared to the as-deposited samples. The interesting thing related to the XRD result is the crystallite size of the samples which is in polycrystalline phase in the as-deposited samples could reach the same particle size as the sample which has an amorphous phase in the as-deposited sample. This result is quite different compared with the XRD result from IO:H layers with different partial pressure of water. It means that the water vapor hold an important role in the development of big particle size in the layer.

If the electrical properties and the XRD result of the layer are correlated, there would be some points that could be taken into account. The carrier density of the sample

has dropped for every sample, which implies that even though the as-deposited sample has crystallized for the sample with thickness of 400nm and 500nm, there is still an amorphous phase that appears in the layer. The drop in the carrier density of the layer became less in the thicker sample and it could be caused by the less amorphous phase which was formed in the thicker layer and leads into an insufficient bonded OH to cover the oxygen vacancy. The mobility result shows that all of the samples have improved mobility after the annealing process even though some of them already in the polycrystalline phase. From the IO:H layers deposited with water vapor series, it is known that the annealing would merely improve the mobility of the IO:H layers which has an amorphous phase in the as-deposited sample. It gave a confirmation that in the 400nm and 500nm thickness, there are still some amorphous phase IO:H in the layer. Since the properties of the layer changes with increasing thickness, the best partial pressure of water for different thickness might be different. The results of different partial pressure of water for IO:H layers with thickness of 200 nm and 400 nm could be seen in Appendix C.

### **3.5. Conclusion**

The result of IO:H layer development has been reported in this chapter. Water vapor plays an important role in the growth of the  $\text{In}_2\text{O}_3$  crystal, which leads into smaller crystallite size. In order to obtain bigger crystallite size, crystallization with vacuum annealing is necessary. After the annealing, IO:H with water vapor being introduced during the deposition reached high mobility above  $100 \text{ cm}^2/\text{Vs}$  and the optimum sheet resistance for the annealed sample with 100nm thickness was  $29 \Omega/\square$ . However, it is not completely clear what might cause the high mobility in the annealed samples and why the mobility could not go higher. The high mobility might be caused by the defects in the layer was clustered during the annealing. It could be possible because the phase of the layer turned from amorphous to polycrystalline. Another reason of the high mobility might be the influence of hydrogen atoms which trapped inside the layer and passivates the oxygen vacancies after the annealing process. After the annealing, the scattering mechanism that might limit the mobility is phonon scattering, which could not be removed from the material.

Going to thicker layer has successfully reduced the sheet resistance of the IO:H layer. However, the obtained sheet resistance is still above  $10\Omega/\square$ . The sheet resistance could reach  $12.5 \Omega/\square$  with 400 nm thickness. It is still a challenge to reduce the sheet resistance even further.



# CHAPTER 4

## Application of IO:H on Thin Film Solar Cells

After understanding the characterization of IO:H, the performance of IO:H as TCO layer in solar cells could be tested. CIGS solar cells were chosen to be the thin film solar cell to test the performance of IO:H layer because it has substrate configuration. It makes the IO:H layer would be the last layer to be deposited before the metal. By doing so, the IO:H layer would not be affected by the other layer deposition which might have various of deposition temperatures and powers. Another reason why CIGS was chosen was it still absorb in the wavelength above visible range. Amorphous silicon solar cell (A-si:H) have been chosen because the deposition of absorber layer is in the range of annealing temperature of IO:H.

### 4.1. CIGS Solar cells

#### 4.1.1. Basic Test Layer

The CIGS solar cell was fabricated at TNO, Eindhoven by Johan Blanker, and brought to Delft to be tested with IO:H as the TCO layer. From previous chapter, it is known that annealing would improve the performance of IO:H layer. Therefore, the annealed IO:H would be tested on top of the solar cells. The problem with annealed IO:H is the entire stack of CIGS solar cells need to be annealed which might change the properties of CIGS. The entire CIGS solar cell was annealed at 200°C for 30 minutes. The structure of both reference CIGS solar cell and CIGS with IO:H as TCO could be seen in figure 23 a and b.

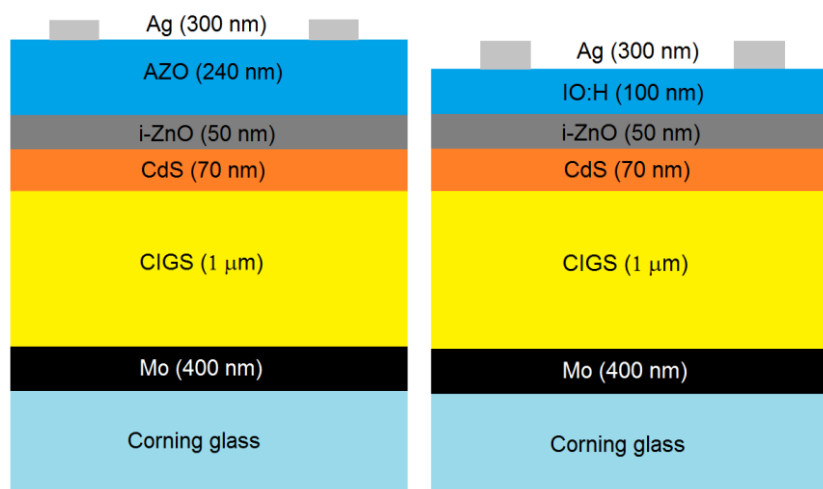


Figure 23.a. Reference CIGS structure b. CIGS with IO:H as TCO

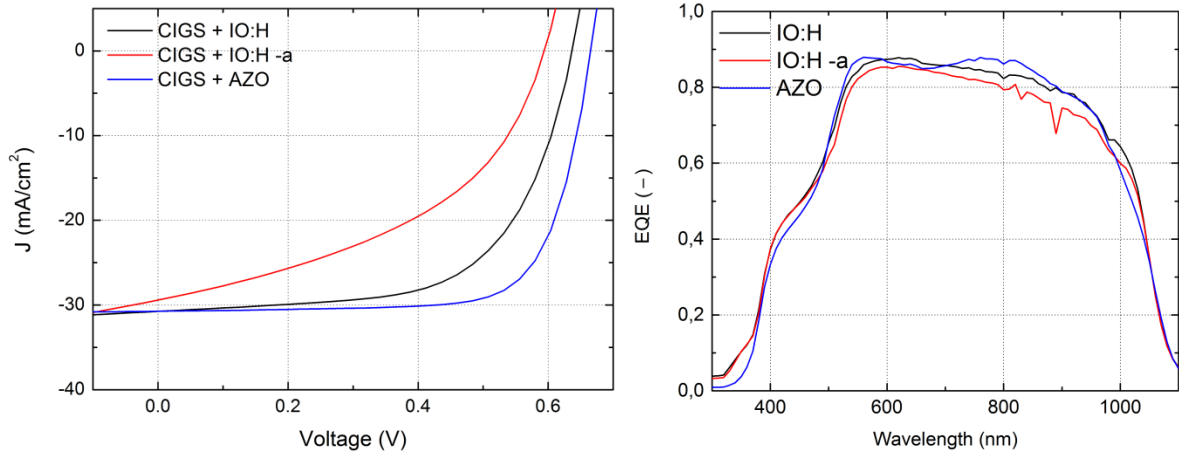


Figure 24. J-V curve and EQE measurement of CIGS solar cells with different TCO

Table 6. Result of CIGS solar cell with different TCO

Device	FF (%)	V <sub>OC</sub> (V)	J <sub>SC</sub> (mA/cm <sup>2</sup> )	R <sub>S</sub> (Ωcm <sup>2</sup> )	R <sub>SH</sub> (Ωcm <sup>2</sup> )	η (%)
<b>CIGS + AZO</b> (3/19)	0.73 ± 0.02	0.67 ± 0.01	30.59	2.3 ± 0.1	1218 ± 530	15.05 ± 0.01
<b>CIGS + IO:H</b> (4/10)	0.58 ± 0.09	0.63 ± 0.05	30.83	3.6 ± 0.2	311.37 ± 142	11.92 ± 0.47
<b>CIGS + IOH</b> <b>Annealed</b> (3/10)	0.43 ± 0.05	0.58 ± 0.02	29.89	85.31 ± 40	113.17 ± 48	7.27 ± 0.7

It could be seen from figure 24 that the CIGS solar cell with IO:H layer on top of it has lower V<sub>OC</sub> and slightly higher J<sub>SC</sub> compared to CIGS solar cell with AZO on top of it. Higher J<sub>SC</sub> in the solar cell with IO:H on top is negligible, compared to the drop in the fill factor and V<sub>OC</sub>. The drop in the V<sub>OC</sub> might be caused by the drop in the shunt resistance (R<sub>SH</sub>), which leads into leakage current in another path. The series resistance (R<sub>S</sub>) of IO:H is higher compared to the series resistance of CIGS with AZO as the TCO. After the annealing process, the V<sub>OC</sub> and fill factor of the CIGS solar cell drop even further, which makes the solar cell perform very bad with efficiency dropped by 4.8%. This is the result of both reduction in the shunt resistance and increase in the series resistance. The summary of the performance of the CIGS solar cells is noted in table 6. The result seems to be unclear, since annealing would lead into a better performance of IO:H layers which is not the case during the application on CIGS solar cell.

#### 4.1.2. Annealing Effect on CIGS Solar Cells

In order to understand the performance of CIGS solar cells better, especially after the annealing, the entire CIGS stack without TCO layer was annealed and then TCO layer was deposited on top of it later on.

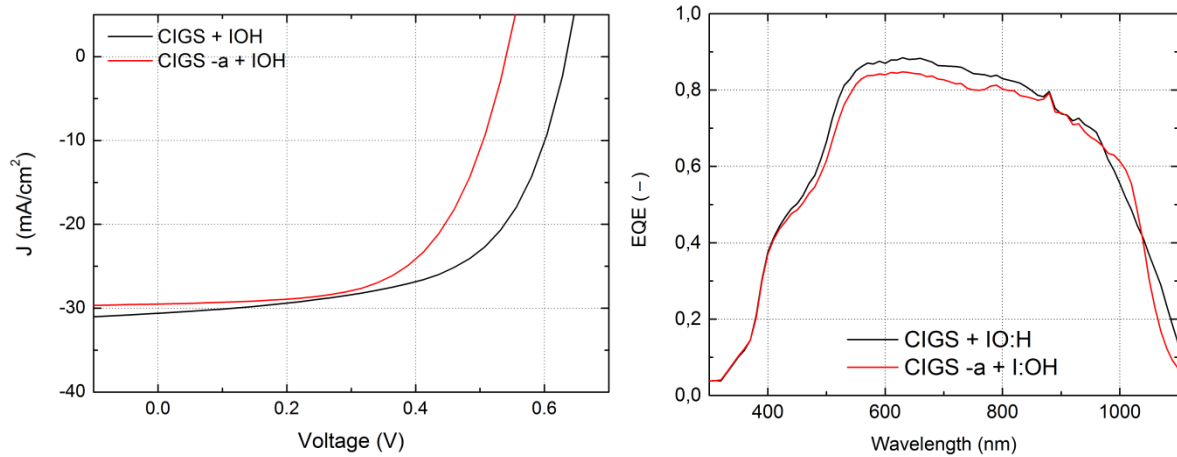


Figure 25. J-V curve and EQE measurement of CIGS solar cell with annealed and as deposited IO:H layer

Table 7. Result of annealing CIGS solar cell

Device	FF (%)	$V_{OC}$ (V)	$J_{SC}$ (mA/cm <sup>2</sup> )	$R_S$ ( $\Omega$ cm <sup>2</sup> )	$R_{SH}$ ( $\Omega$ cm <sup>2</sup> )	$\eta$ (%)
<b>CIGS + IO:H</b> (4/10)	$0.58 \pm 0.09$	$0.63 \pm 0.05$	30.83	$3.6 \pm 0.2$	$311.37 \pm 142$	$11.92 \pm 0.47$
<b>CIGS annealed + IOH</b> (3/10)	$0.51 \pm 0.9$	$0.53 \pm 0.03$	29.97	$4.5 \pm 0.8$	$342.37 \pm 285$	$8.2 \pm 1.8$

The CIGS solar cell which annealed have lower  $V_{OC}$ ,  $J_{SC}$ , and fill factor, resulting in lower the efficiency of the cell by 3.7% compared to the CIGS solar cell with IO:H layer without any temperature treatment. It might indicate that the CIGS was partially damaged during the annealing. This is might be caused by the Cadmium in the CdS layer diffused further to the CIGS layer, which makes the p-n junction become less effective. The annealed CIGS has slightly higher series resistance but higher shunt resistance compared to as-deposited CIGS. It makes the damaged CIGS does not influence the value of both series resistance and shunt resistance relatively. One thing that might affect the series resistance is the physical contact between the annealed IO:H - the metal contact or annealed IO:H - iZnO since the phase of the layer change from amorphous to polycrystalline. While the shunt resistance might be the effect of the inappropriate band alignment between IO:H

layer – iZnO since all of the solar cells with IO:H layers will have typical shunt resistance in the value of  $300 \Omega/\text{cm}^2$ .

#### 4.1.3. Effect of ITO

It is known from the literature that the contact between IO:H and silver as the metal grid might cause a lower fill factor and  $V_{OC}$ , even though the  $J_{SC}$  could be increased. Especially after the annealing of IO:H with silver on top of it. This is due to the formation of AgO in the interface between IO:H and silver [13]. Therefore, introduction of ITO layer as an intermediate layer between IO:H and silver was applied. The structure of CIGS with ITO as intermediate layer could be seen in figure 26.

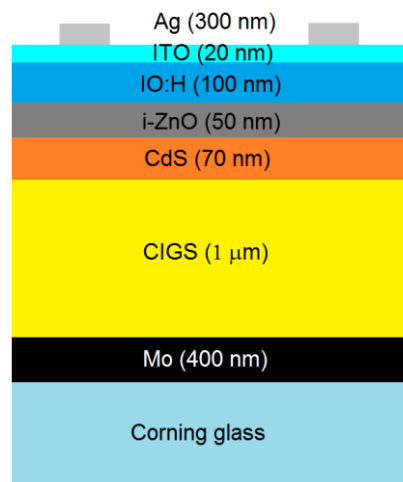


Figure 26. CIGS with IO:H and ITO as TCO

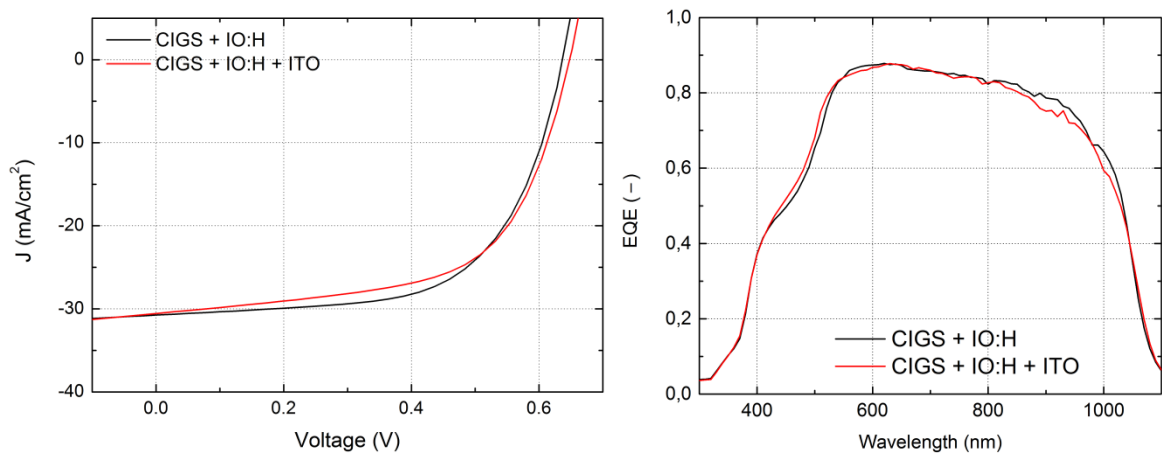


Figure 27. J-V curve and EQE measurement of CIGS solar cell with ITO intermediate layer

**Table 8. Result of CIGS solar cell with ITO intermediate layer**

Device	FF (%)	V <sub>OC</sub> (V)	J <sub>SC</sub> (mA/cm <sup>2</sup> )	R <sub>S</sub> (Ωcm <sup>2</sup> )	R <sub>SH</sub> (Ωcm <sup>2</sup> )	η (%)
<b>CIGS + IO:H (4/10)</b>	0.58 ± 0.09	0.63 ± 0.05	30.83	3.6 ± 0.2	311.37 ± 142	11.92 ± 0.47
<b>CIGS + IO:H + ITO (6/10)</b>	0.60 ± 0.09	0.65 ± 0.01	31.34	3.6 ± 0.9	313.33 ± 239	12.7 ± 0.7

The result in figure 26 was summarized in table 9. The fill factor, J<sub>SC</sub>, and V<sub>OC</sub> of the CIGS solar cell were increased after ITO intermediate layer introduced. It leads into the increase of overall efficiency by 0.8%. From the EQE result, it could be seen that CIGS with ITO intermediate layer have lower EQE in the longer wavelength compared to CIGS without ITO intermediate layer. This is due to that ITO is more absorbing in the NIR region.

#### 4.2. Amorphous Silicon Solar Cells

The experiment of the IO:H on top of amorphous silicon solar cells was done by Fai Tong Si, colleague in PVMD group. Since the a:Si:H solar cells has a superstrate configuration, the IO:H layer will be annealed during the deposition of absorber layer. The substrate deposition temperature of the absorber layer was 180 °C. The structure of a-Si:H solar cell with AZO and with IO:H could be seen in figure 28 a and b.

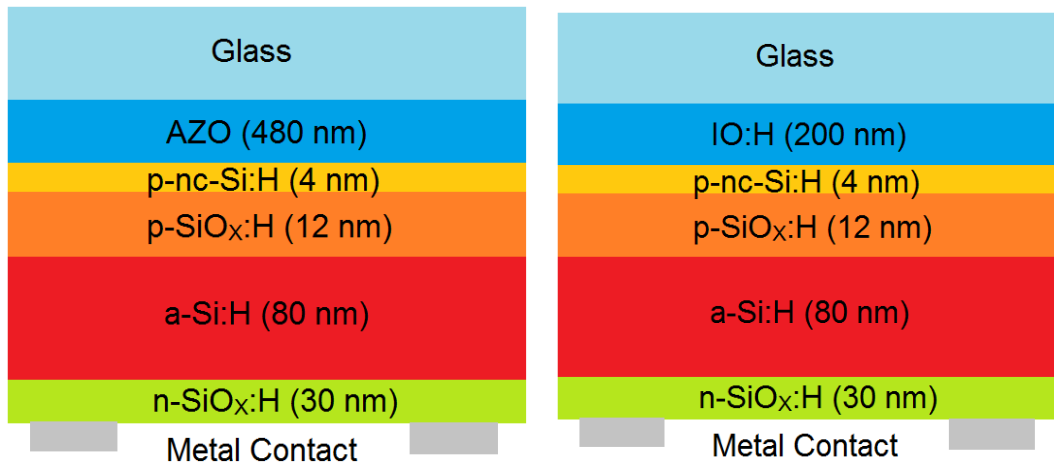


**Figure 28. a-Si:H solar cell structure with a. AZO and b. IO:H as front TCO**

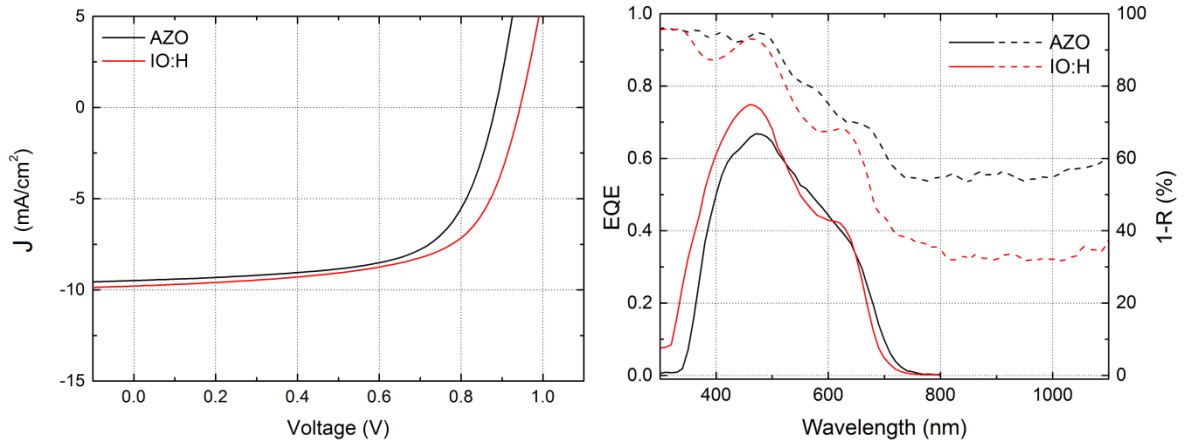


Figure 29. a. J-V curve and EQE result of a-Si:H solar cell with different TCO

Figure 29a shows that the a-Si:H solar cell with IO:H layer as TCO has better  $V_{OC}$  and  $J_{SC}$  compared to the a-Si:H solar cell with AZO as TCO layer. However, the fill factor of the solar cell with IO:H layer is lower compared to solar cell with AZO as TCO. Figure 29b shows the EQE result of both solar cells. After the maximum absorption wavelength of a-Si:H solar cell at 800nm, it could be seen that the solar cell with IO:H layer have lower 1-R value compared to solar cell with AZO layer. This is due to lower carrier density of IO:H layer which lead into lower plasma frequency. Table 9 summarize the comparison between a-Si:H solar cells with AZO and IO:H as the TCO layer.

Table 9. Application of IO:H on a-Si solar cell

Device	FF (%)	$V_{OC}$ (V)	$J_{SC}$ (mA/cm <sup>2</sup> )	$R_s$ ( $\Omega\text{cm}^2$ )	$R_{SH}$ ( $\Omega\text{cm}^2$ )	$\eta$ (%)
a-si + AZO (11/14)	$0.64 \pm 0.01$	$0.88 \pm 0.01$	9.49	7.7	945	$5.34 \pm 0.01$
a-si + IO:H (7/14)	$0.61 \pm 0.03$	$0.93 \pm 0.03$	9.79	8.6	1007	$5.63 \pm 0.47$

### 4.3. Conclusion

IO:H application on CIGS solar cells and single junction a-Si:H solar cells has been reported in this chapter. The application in CIGS solar cells shows that the IO:H shows lower performance compared to AZO, especially if the IO:H was annealed together with the CIGS solar cell. However, the intermediate thin ITO layer could improve the performance of CIGS solar cells with IO:H. The IO:H application in a-Si:H solar cell shows promising results as it has higher  $V_{OC}$  and  $J_{SC}$  than a-Si:H solar cell with AZO as TCO. However, the common thing from IO:H as TCO is the drop in the fill factor which should be tackled in the future.

# CHAPTER 5

## Conclusion and Recommendation

### 5.1. Conclusion

The effects of water vapor, thickness and annealing temperature have been examined in this report. The water vapor suppresses the growth of the  $\text{In}_2\text{O}_3$  crystal and makes the layer deposited in amorphous phase. Introduction of water vapor will make the IO:H layer more conductive with the lowest resistivity of  $3.4 \times 10^{-4} \Omega/\text{cm}$  could be achieved. The mobility of sample with water vapor stabilizes at the value of  $60 \text{ cm}^2/\text{Vs}$ . Moreover, the water vapor will increase the optical band gap of IO:H layer. In order to obtain high mobility, solid phase crystallization by vacuum annealing has been performed. The amorphous IO:H layer will be crystallized with random orientation after the annealing. Annealing increase the mobility of IO:H with the optimum value of mobility about  $150 \text{ cm}^2/\text{Vs}$ . There are a suggestion to answer the reason behind high mobility in IO:H TCO. The formation of cluster between  $V_{\text{In}}$  and  $V_{\text{O}}$  which reduce the scattering mechanism caused by both might be the reason to obtain high mobility. The formation of cluster of defects might be possible due to the phase change from amorphous phase into polycrystalline phase during the annealing. There are some other parameter that limits the mobility such as phonon scattering which could not be removed and defects caused vacancies.

Increasing the thickness of IO:H will leads into the change of amorphous phase into polycrystalline phase. The resistivity of the layer increased linearly with the increment of the thickness, while the sheet resistance of the IO:H layers will form a plateau which stabilizes around  $13 \Omega/\square$  at thickness of 400nm. The mobility of IO:H layer with thickness between 200 nm to 500 nm stabilize at  $60 \text{ cm}^2/\text{Vs}$  in the as-deposited samples and  $120 \text{ cm}^2/\text{Vs}$  in the annealed samples. There are still some improvement that might be done to improve the properties of IO:H layer to obtain a value of sheet resistance  $<10 \Omega/\square$ .

The application of IO:H layer on top of CIGS solar cells shows that it needs to be optimized further. Replacing AZO with IO:H on top of CIGS solar cells reduced the efficiency of the CIGS solar cell by 3.1%. This is due to the lower  $V_{\text{OC}}$  and fill factor of the solar cell, which might be caused by the drop of the shunt resistance. The  $J_{\text{SC}}$  of CIGS with IO:H on top of it shows slight improvement and it might be the lower absorbance of IO:H in the NIR region compared to AZO. Introducing intermediate ITO layer between the IO:H

and silver results in some improvement to tackle the bad contact between IO:H and silver. However, the annealing process which could improve the IO:H performance could not be applied in CIGS solar cell since it would degrade the CIGS solar cell itself. The a-Si:H solar cell with IO:H as TCO shows a better performance compared to a-Si:H solar cell with AZO as TCO with increased of efficiency by 0.3%

## **5.2. Recommendation**

According to the work from Koida et al. [26], the introduction of oxygen flow during deposition could reduce the number of Oxygen vacancies in the layer. The reduction of the oxygen vacancies would reduce the factors which limit the mobility as well. Therefore the optimization and understanding of oxygen flow during deposition will be important for improving the mobility of IO:H layer.

Effect of annealing might be interesting to be investigated further, since the processing of solar cell might have a lot of variety temperature, power and method of deposition which might influence the performance of the solar cell. Another thing that might be interested to be tested further would be the stability of IO:H layer, since it might be necessary in the application. The stability of IO:H layer are still being tested by Anusha Varanasi, colleague in PVMD group.

Application of IO:H layer for solar cell application or for the other application might be interesting to be investigated. This is due to the compatibility of IO:H layer with the other material used for any application might be different.

## References

- [1] “Energy [R]evolution | Greenpeace Philippines.” [Online]. Available: <http://www.greenpeace.org/seasia/ph/What-we-do/Climate-and-Energy/energyrevolution/>.
- [2] C. Bright, *Transparent conductive thin films*. Woodhead Publishing Limited, 2013.
- [3] T. O. M. T.J. Coutts, J.D. Perkins, and D.S. GinleyMason, “Transparent Conducting Oxides : Status and Opportunities in Basic,” *195th Meet. Electrochem. Soc.*, no. August, 1999.
- [4] H. Liu, V. Avrutin, N. Izyumskaya, Ü. Özgr, and H. Morkoç, “Transparent conducting oxides for electrode applications in light emitting and absorbing devices,” *Superlattices Microstruct.*, vol. 48, no. 5, pp. 458–484, 2010.
- [5] T. Minami, “Substitution of transparent conducting oxide thin films for indium tin oxide transparent electrode applications,” *Thin Solid Films*, vol. 516, no. 7, pp. 1314–1321, 2008.
- [6] T. Minami, “Transparent conducting oxide semiconductors for transparent electrodes,” *Semicond. Sci. Technol.*, vol. 20, no. 4, pp. S35–S44, 2005.
- [7] T. Koida, H. Fujiwara, and M. Kondo, “Hydrogen-doped  $\text{In}_2\text{O}_3$  as high-mobility transparent conductive oxide,” *Japanese J. Appl. Physics, Part 2 Lett.*, vol. 46, no. 25–28, pp. 18–21, 2007.
- [8] “Solar Applied Materials Technology Corporation.” [Online]. Available: [http://www.solartech.com.tw/en/product\\_sputtering\\_targets\\_for\\_thin\\_film\\_solar\\_cell\\_101.html](http://www.solartech.com.tw/en/product_sputtering_targets_for_thin_film_solar_cell_101.html).
- [9] H. Tan, P. Babal, M. Zeman, and A. H. M. Smets, “Wide bandgap p-type nanocrystalline silicon oxide as window layer for high performance thin-film silicon multi-junction solar cells,” *Sol. Energy Mater. Sol. Cells*, vol. 132, no. October 2014, pp. 597–605, 2015.
- [10] “Perovskites and Perovskite Solar Cells: An Introduction – Ossila.” [Online]. Available: <https://www.ossila.com/pages/perovskites-and-perovskite-solar-cells-an-introduction>.
- [11] “a-Si/c-Si Heterojunction Solar Cells.” [Online]. Available: [http://pvlab.epfl.ch/heterojunction\\_solar\\_cells](http://pvlab.epfl.ch/heterojunction_solar_cells). [Accessed: 01-Jan-2016].
- [12] E. Fortunato, D. Ginley, H. Hosono, and D. C. Paine, “Transparent Conducting Oxides for Photovoltaics,” *MRS Bull.*, vol. 32, no. March, pp. 242–247, 2007.
- [13] L. Barraud, Z. C. Holman, N. Badel, P. Reiss, a. Descoedres, C. Battaglia, S. De Wolf, and C. Ballif, “Hydrogen-doped indium oxide/indium tin oxide bilayers for high-efficiency silicon heterojunction solar cells,” *Sol. Energy Mater. Sol. Cells*, vol. 115, pp. 151–156, 2013.

- [14] T. Koida and M. Kondo, "Comparative studies of transparent conductive Ti-, Zr-, and Sn-doped  $\text{In}_2\text{O}_3$  using a combinatorial approach," *J. Appl. Phys.*, vol. 101, no. 6, 2007.
- [15] S. Limpijumng, P. Reunchan, A. Janotti, and C. G. Van De Walle, "Hydrogen doping in indium oxide: An ab initio study," *Phys. Rev. B - Condens. Matter Mater. Phys.*, vol. 80, no. 19, pp. 1–4, 2009.
- [16] T. Koida and M. Kondo, "Improved near-infrared transparency in sputtered  $\text{In}_2\text{O}_3$ -based transparent conductive oxide thin films by Zr-doping," *J. Appl. Phys.*, vol. 101, no. 6, pp. 4–8, 2007.
- [17] S. Calnan and a. N. Tiwari, "High mobility transparent conducting oxides for thin film solar cells," *Thin Solid Films*, vol. 518, no. 7, pp. 1839–1849, 2010.
- [18] I. a. Rauf, "Extraction of free carrier density and mobility from the optical transmission data of tin-doped indium oxide thin films," *Mater. Lett.*, vol. 23, no. 1–3, pp. 73–78, 1995.
- [19] K. Ellmer, A. Klein, and B. Rech, *Transparent Conductive Zin Oxide Basic and Applications in Thin Film Solar Cells*. 2008.
- [20] G. J. Exarhos and X.-D. Zhou, "Discovery-based design of transparent conducting oxide films," *Thin Solid Films*, vol. 515, no. 18, pp. 7025–7052, 2007.
- [21] F. U. Hamelmann, "Transparent Conductive Oxides in Thin Film Photovoltaics," *J. Phys. Conf. Ser.*, vol. 559, p. 012016, 2014.
- [22] T. Koida, H. Fujiwara, and M. Kondo, "Structural and electrical properties of hydrogen-doped  $\text{In}_2\text{O}_3$  Films Fabricated by Solid-Phase Crystallization," *J. Non. Cryst. Solids*, vol. 354, no. 19–25, pp. 2805–2808, 2008.
- [23] H. Nakazawa, Y. Ito, E. Matsumoto, K. Adachi, N. Aoki, and Y. Ochiai, "The electronic properties of amorphous and crystallized  $\text{In}_2\text{O}_3$  films," *J. Appl. Phys.*, vol. 100, no. 9, p. 093706, 2006.
- [24] R. L. Weiher, "Electrical properties of single crystals of indium oxide," *J. Appl. Phys.*, vol. 33, no. 9, pp. 2834–2839, 1962.
- [25] Z. Galazka, K. Irscher, M. Pietsch, T. Schulz, R. Uecker, D. Klimm, and R. Fornari, "Effect of heat treatment on properties of melt-grown bulk  $\{\text{In}_2\text{O}_3\}$  single crystals," *CrystEngComm*, vol. 15, pp. 2220–2226, 2013.
- [26] T. Koida, H. Shibata, M. Kondo, K. Tsutsumi, A. Sakaguchi, M. Suzuki, and H. Fujiwara, "Correlation between oxygen stoichiometry, structure, and opto-electrical properties in amorphous  $\text{In}_2\text{O}_3\text{:H}$  films," *J. Appl. Phys.*, vol. 111, no. 6, 2012.
- [27] W. Xiao and W. G. Dunford, "A modified adaptive hill climbing MPPT method for photovoltaic power systems," in *PESC Record - IEEE Annual Power Electronics Specialists Conference*, 2004, vol. 3, pp. 1957–1963.

- [28] T. Koida, M. Kondo, K. Tsutsumi, A. Sakaguchi, M. Suzuki, and H. Fujiwara, "Hydrogen-doped In<sub>2</sub>O<sub>3</sub> transparent conducting oxide films prepared by solid-phase crystallization method," *J. Appl. Phys.*, vol. 107, no. 3, 2010.
- [29] B. Macco, H. C. M. Knoops, and W. M. M. Kessels, "Electron Scattering and Doping Mechanisms in Solid-Phase-Crystallized In<sub>2</sub>O<sub>3</sub>:H Prepared by Atomic Layer Deposition," *ACS Appl. Mater. Interfaces*, vol. 7, no. 30, pp. 16723–16729, 2015.
- [30] H. F. Wardenga, M. V. Frischbier, M. Morales-Masis, and A. Klein, "In situ hall effect monitoring of vacuum annealing of In<sub>2</sub>O<sub>3</sub>:H thin films," *Materials (Basel)*, vol. 8, no. 2, pp. 561–574, 2015.
- [31] P. Reunchan, X. Zhou, S. Limpijumnong, A. Janotti, and C. G. Van De Walle, "Vacancy defects in indium oxide: An ab-initio study," *Curr. Appl. Phys.*, vol. 11, no. 3 SUPPL., pp. S296–S300, 2011.
- [32] S. K. Chong, S. N. A. Azizan, K. W. Chan, H.-Q. Nguyen, W. S. Chiu, Z. Aspanut, C. F. Dee, and S. A. Rahman, "Structure deformation of indium oxide from nanoparticles into nanostructured polycrystalline films by in situ thermal radiation treatment," *Nanoscale Res. Lett.*, vol. 8, no. 1, p. 428, 2013.
- [33] H. Fujiwara and M. Kondo, "Effects of carrier concentration on the dielectric function of ZnO:Ga and In<sub>2</sub>O<sub>3</sub>:Sn studied by spectroscopic ellipsometry: Analysis of free-carrier and band-edge absorption," *Phys. Rev. B - Condens. Matter Mater. Phys.*, vol. 71, no. 7, pp. 1–10, 2005.
- [34] I. Makkonen, E. Korhonen, and V. Prozheeva, "Identification of vacancy defect complexes in transparent semiconducting oxides: the cases of ZnO, In<sub>2</sub>O<sub>3</sub> and SnO<sub>2</sub>," *J. Phys. Condens. Matter*, vol. 224002, no. August, p. 224002, 2016.
- [35] F. Reurings, C. Rauch, F. Tuomisto, R. E. Jones, K. M. Yu, W. Walukiewicz, and W. J. Schaff, "Defect redistribution in postirradiation rapid-thermal-annealed InN," *Phys. Rev. B - Condens. Matter Mater. Phys.*, vol. 82, no. 15, pp. 1–4, 2010.
- [36] K. M. Johansen, a. Zubiaga, F. Tuomisto, E. V. Monakhov, a. Y. Kuznetsov, and B. G. Svensson, "H passivation of Li on Zn-site in ZnO: Positron annihilation spectroscopy and secondary ion mass spectrometry," *Phys. Rev. B - Condens. Matter Mater. Phys.*, vol. 84, no. 11, pp. 1–4, 2011.
- [37] B. Macco, M. a. Verheijen, L. E. Black, B. Barcones, J. Melskens, and W. M. M. Kessels, "On the solid phase crystallization of In<sub>2</sub>O<sub>3</sub>:H transparent conductive oxide films prepared by atomic layer deposition," *J. Appl. Phys.*, vol. 120, no. 8, p. 085314, 2016.
- [38] R. Green, "Hall Effect Measurements in Materials Characterization," *White Pap.*, no. 440, pp. 1–12, 1879.
- [39] Keithley, "Four-Probe Resistivity and Hall Voltage Measurements with the Model 4200-SCS," 2007.

- [40] E. Garcia-Caurel<sup>1</sup>, A. De Martino<sup>1</sup>, J-P. Gaston<sup>2</sup>, and L. Yan<sup>3</sup>, “Application of Spectroscopic Ellipsometry and Mueller Ellipsometry to Optical Characterization.”
- [41] R. M. a. Azzam, “Ellipsometry,” *Handb. Opt. Third Ed. Vol. I Geom. Phys. Opt. Polariz. Light. Components Instruments*, pp. 1–26, 2009.
- [42] D. Gonçalves and E. Irene, “Fundamentals and applications of spectroscopic ellipsometry,” *Quim. Nova*, vol. 25, no. 5, pp. 794–800, 2002.
- [43] J. Palmer, “Chapter 25: The measurement of transmission, absorption, emission, and reflection,” *Handb. Opt.*, pp. 1–25, 1995.
- [44] F. Padera, “Measuring Absorptance (k) and Refractive Index (n) of Thin Films with the PerkinElmer Lambda 950/1050 High Performance UV-Vis/NIR Spectrometers,” *PerkinElmer, Inc.*, pp. 1–9, 2013.
- [45] M. Birkholz, *Thin Film Analysis by X-Ray Scattering*. Wiley-VCH Verlag GmbH & Co. KGaA, 2006.
- [46] E. Smith and G. Dent, *Modern Raman Spectroscopy - A Practical Approach*. 2005.
- [47] I. Procházka, “Positron Annihilation Spectroscopy,” *Mater. Struct.*, vol. 8, no. 2, pp. 55–60, 2001.
- [48] R. Krause-Rehberg, “Fundamentals of positron annihilation spectroscopy and its application in semiconductors,” 2014.

## Acknowledgements

I would like to thank my examination committee for their time and efforts on reading my thesis. I would like to thank Olindo to allow me join Photovoltaic and Material Devices (PVMD) group and working on my thesis here. Olindo, you always push me to the limit, and you show me how to work with high determination. I would also like to thank Andrea to always be there to give me feedback and help me to solve the problem. Andrea, I learn a lot of thing from you, especially how to become a world class researcher, I'm really happy having you as my daily supervisor. I would like to thank Johan Blanker and Fai Tong Si for helping me with the fabrication of solar cells. The experimental work cannot be done by the help from the technician of PVMD group, Martijn and Stefaan. I would like to say that you two are the best technician that I've ever work with, your experience and your capabilities are not questionable. I would like to thank Yi Hsiu, for helping me with analysis of CIGS and for being a good office mate who always shares her food with me, more importantly, thank you for give me your time to proofread my thesis. I would like to thank all of the PVMD group member that I cannot mention one by one. I would also like to thank Stephan and Marteen whose helping me for the PAS characterization, and Valeria Russo for helping me with Raman Spectroscopy characterization. Last but not least, I would like to thanks Winda for proofreading my thesis.

I would like to thank my uncle and aunt, Kulyong and Kuyang, thanks for having me, always taking care of me, and let me stay at your home. I know will never be able to return your help to me during my stay in Netherland. I would like to thank my cousins, Priscilla and Samuel, thanks to always make a joke about me so I can think harder to make fun of you two. I would like to thank my parents, for let me choose what I want to do in life and let me explore the world. Thank you for always be there back me up every time things get harder here. I would like to thank Titi, Arlin, and Adi, for always be there to support me.

I would like to thank all of my friend that gave me precious time during my study in Netherland. I would like Indonesian student association in Delft (PPI Delft) for always make Delft as comfortable as home with a lot of activities. I would like to thank Ricardo, Anandro, Theo, Dimas, and Hafida to always support me during my thesis. We should make a meeting for all of us. Thank you to friend whose study in EEMCS building for help me relieving stress by playing foosball and always be there during lunch time so I can forget about thesis for a moment.

20th October 2016

Delft, the Netherlands

Ariyanto Wibowo



# Appendix A

## Characterization Setup

### A.1. Hall Setup

Hall Effect measurement becomes an important tool for material characterization since Edwin Hall discovered the phenomenon. The Hall Effect could be observed in a combination of magnetic field through a sample and a current along the length of the sample that would create a transverse voltage perpendicular to both the magnetic field and the current. The Basic Principle of the measurement is the Lorentz force, the force on a point charge due to electromagnetic fields. Nowadays, the modern semiconductor material are no longer bulk materials, they often come in the form of thin films which lead the manufacturer to go back to determine carrier concentration and carrier mobility independently. It makes the application of Hall Effect measurements are ideal. The interest in the Hall Effect is growing related to the amount of current that could be handled by a device. If the current could be maximized, than the device could be operated in lower power level, switch faster, and have higher bandwidth.

The special thing about Hall Effect measurement is the possibilities to measure mobility of a sample. The first step to measure Hall Voltage ( $V_H$ ) is forcing both magnetic field perpendiculars to the sample and a current through the sample. Combination of both current flow ( $I$ ) and magnetic field ( $B$ ) would cause a transverse current. The  $V_H$  would be measured across the sample. To obtain accurate mobility measurement, both the sample thickness ( $t$ ) and its resistivity ( $\rho$ ) would be required. Afterwards, the Hall mobility could be calculated by using equation 6:

$$\mu_H = \frac{|V_H \times t|}{B \times I \times \rho} \quad (6)$$

Where:  $\mu_H$  = Hall Mobility ( $\text{cm}^2/\text{Vs}$ )

$V_H$  = Hall Voltage (V)

$t$  = Sample Thickness (cm)

$B$  = Magnetic Field (T)

$I$  = Current Flow (A)

$\rho$  = Resistivity ( $\Omega\text{cm}$ )

The right measurement to obtain hall voltage is needed because it has a big influence to the calculation of Hall mobility. In purpose to get a exact result of the

measurement, there are three things that should be done, the combination of reversing source current polarity; sourcing on additional terminal and reversing direction of the magnetic field. After all of the measurement, the average of the measured voltage needs to be calculated.

$$V_C = V_{24P} - V_{24N} \qquad V_E = V_{13P} - V_{13N}$$

$$V_D = V_{42P} - V_{42N} \qquad V_F = V_{31P} - V_{31N}$$

$$V_H = (V_C + V_D + V_E + V_F) / 8$$

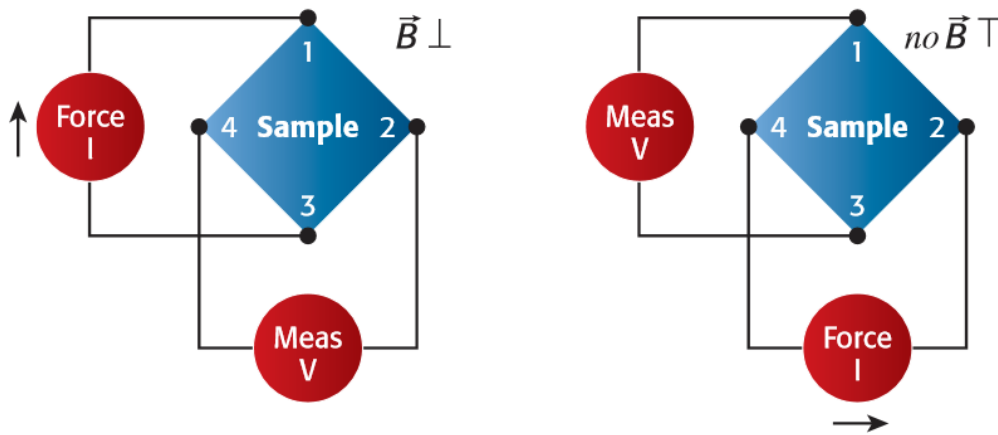


Figure 30. Scheme of Hall voltage measurement with both positive and negative polarity current, both magnetic field up and down, and both configuration [38]

Other properties that might affect the hall measurement are temperatures of the substrate. It is highly recommended to monitor the temperature of the substrate during measurement, especially application which includes multiple time measurement. One solution that might be done is adjustment of the temperature by using a prober chuck that could heat up or cool down the sample or temperature measuring probe which has 0,1°C resolution.[38]

## A.2. Four Point Probe

One of important properties that need to be known in semiconductor material is resistivity. Resistivity could affect the capacitance, the series resistance, and the threshold voltage in the application for a device. The equipment that is commonly used to measure resistivity is a four-point probe. During the measurement, two probes are used to be the current source, and the other two probes are used to measure the voltage in the technique that is called four-probe or kelvin technique. By using four probes during the measurement, the errors due to probe resistance, spreading resistance under each probe, and the metal contact between the probe and the material could be eliminated. Besides, the errors could be eliminated because the use of high impedance voltmeter which draw a very small

amount of current. The small amount of current leads into a very small drop voltage across the probe. There are two common four-probe techniques to determine resistivity of semiconductor material, i.e., the four-point collinear probe method and the Van der Pauw method.[39]

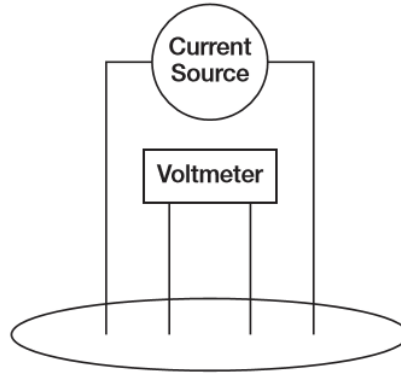


**Figure 31. Scheme of four-point collinear probe [39]**

The four-point collinear probe is easier to implement compared to the van der Pauw method. The scheme of the measurement could be found in Figure 31. Two probes that are used for the current source are two outer probes. The inner probes are used as voltmeter to measure the voltage drop across the surface of the sample. The Volume Resistivity could be calculated as

$$\rho = \frac{\pi}{\ln 2} \times \frac{V}{I} \times t \times k \quad (7)$$

Where:  $\rho$  = Volume Resistivity ( $\Omega\text{cm}$ )

$V$  = Measured Voltage (V)

$I$  = The source Current (A)

$t$  = Thickness (cm)

$k^*$  = a correction factor based on the ratio of the probe to wafer diameter and on the ratio of wafer thickness to probe separation

### **A.3. Spectroscopy Ellipsometry**

Ellipsometry is a method to gain information related to physical properties of a sample from indirect optical technique and modeling analysis. Standard ellipsometry device is commonly used to characterize a material that either optically isotropic bulk and/or layered. The advantages of using ellipsometry compared to reflectometry are the measurement of two different values for every wavelength that allows the setup to gain more information to analyze thin film measurement accurately. [40] The basic principles of

ellipsometry are measurement of changes in state of polarization of light upon reflection for the in-situ and real-time characterization of surfaces, interfaces, and thin films. Collimated beam of monochromatic or quasi-monochromatic light, that have been polarized in a known state, is incident of a sample surface that is going to be examined, and the state of polarization of reflected light is going to be analyzed too. From both incident and reflected polarization, ratios of complex reflection coefficient of the surface for the orthogonal linear polarization and perpendicular polarization to the plane of incident are determined. These ratios are subsequently related to the structural and optical properties of the ambient-sample interface region by invoking an appropriate model and the electromagnetic theory of reflection. [41]

Two copropagating orthogonally polarized waves could be considered to act as a reference for each other. The state of polarization is determined by the superposition of the orthogonal components of electric field vector, which defines an ellipsometer might be thought as a polarization interferometer. Another advantage of using ellipsometry is it only involves relative amplitude and relative phase measurement which makes it is highly accurate. The other advantage is its sensitivity to minute change in the interface region, such as the formation of monolayer of atoms or molecules that makes it is suitable for many applications in surface science and thin-film technologies. [41]

The typical scheme, the incident light is linearly polarized as a known but arbitrary azimuth and the reflected light is elliptically polarized. The incident light is linearly polarized with the electric vector vibrating parallel top or perpendicular s to the plane of incidence, the reflected light is likewise p- and s- polarized, or the p and s polarizations are the eigenpolarizations or reflection. Measurement of the ellipse of polarization of reflected light accounts for the name ellipsometry. [41] The scheme of the setup could be seen in figure 32.

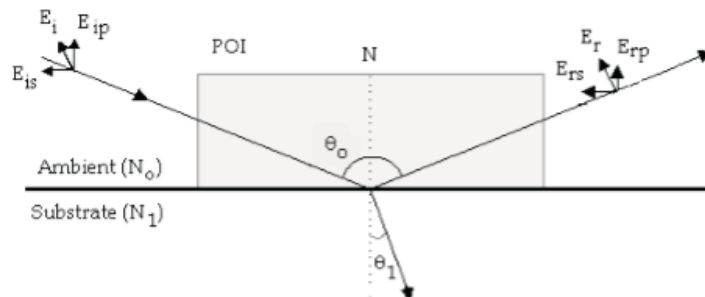


Figure 32. Scheme of Spectroscopic Ellipsometry [42]

#### A.4. Reflectance and Transmittance

Three processes occurred when radiant flux is incident upon a surface or medium, which are transmission, reflection, and absorption. Figure 33 shows ideal case of reflectance and transmittance, both of them might have a specular or perfectly diffuse component.

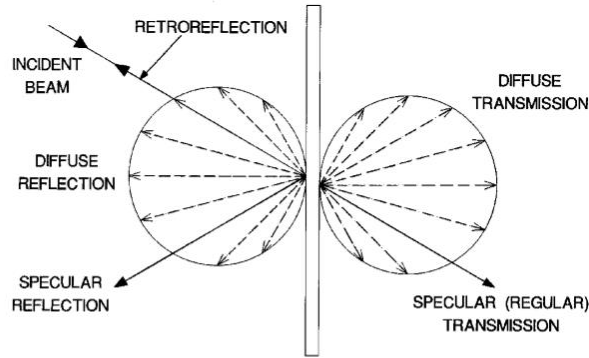


Figure 33. Ideal reflection and transmission[43]

To measure transmittance and reflectance, a spectrophotometer with integrating sphere had been used. The scheme of spectrophotometer with integrating sphere could be found in figure 34. For the transmittance measurement, the sample was placed in front of the integrating sphere, at the transmittance port, and put in either a calibrated mirror or a labsphere calibrated spectralon standard which has a specific calibration sheet for that standard at the sample reflectance port. The purpose of using mirror or spectralon is to obtain total transmission of the sample. For reflectance measurement, the sample was placed at sample reflectance port. Two things that needed to be taken into account during reflectance measurement are the reflectance need to be measured in absolute %R, which means the spectra are corrected for the reflectance of reference material (light spectral reference), therefore a calibrated mirror, spectralon, or a certain material might be used during the measurement. The correction is being needed for the dark level (0%R) of the sphere (dark Spectral Reference).

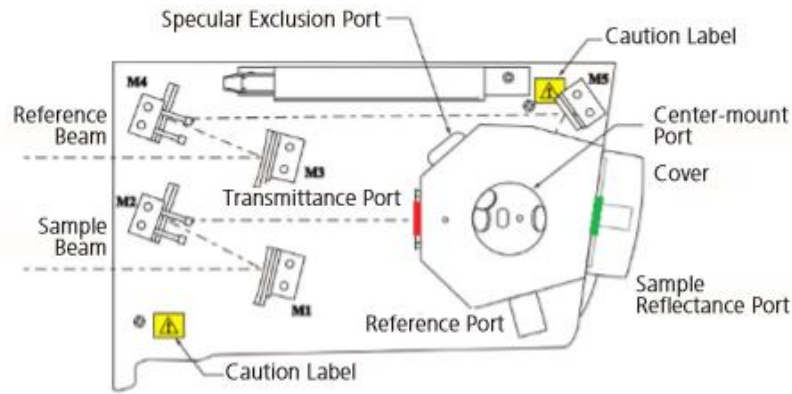


Figure 34. Scheme of spectrophotometer with integrating sphere[44]

### A.5. X-ray Diffraction

One phenomenon that appears when electromagnetic radiation impinges on periodic structure with geometrical variations on the length scale of the wavelength of the radiation is diffraction. The interatomic distances in crystals and molecules amount to 0.15-0.4 nm which correspond in the electromagnetic spectrum with the wavelength of x-rays have photon energy between 3 to 8 KeV. Constructive and destructive interference phenomena should be observed when crystalline and molecular structure is exposed to x-rays. There are three different types of interaction in the relevant energy range. First, electron might be liberated from their bound atomic states in the process photoionization. This process occurs due to the energy and the momentum from the incoming radiations which are transferred to the excited electron. This process results photoionization becomes the group of inelastic scattering processes. The second process is Compton scattering, this process also includes in inelastic scattering but the incoming x-ray beams might be undergo. In the Compton Scattering, the energy is also transferred into an electron, but without releasing the electron from the atom. The third process, which incoming x-rays beam could be scattered elastically by electron, is called Thomson scattering. In this process, electron oscillates like a Hertz dipole at the frequency of the incoming beam and becomes the source of dipole radiation. One approximation that suitable to approach when the distances between scattering objects are much smaller than the distance to the measurement point is Fraunhofer diffraction.

$$2 d \sin\theta = n\lambda \quad (8)$$

Where:  $d$  = Distance between atomic layers in crystal

$\theta$  = Angles of incidences

$n$  = Integer

$\lambda$  = Wavelength of the incident X-ray beam

The equation 8 is called Bragg equation; it was applied by W.H. Bragg and W.L. Bragg in 1913 to determine the position of x-ray scattering peaks in angular space. [45] This observation is an example of x-ray wave interference or commonly known as x-ray diffraction (XRD). It was a direct evidence for the periodic atom structure of crystals postulated for several centuries.

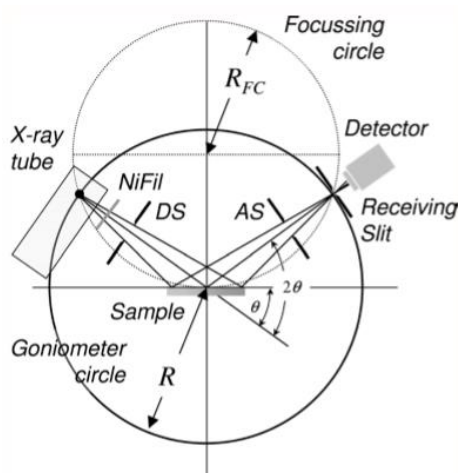


Figure 35. Geometry of XRD instrument [45]

Figure 35 shows a basic geometry of by far the most frequently used x-ray diffraction instrument. The sample should be placed in a plane or flattened surface. The incoming and exiting beam have angle of  $\theta$  with respect to the sample surface. The data that would be collected are the diffraction pattern of the incoming x-ray beam with variation of incoming angle  $\theta$  and the scattering angle by  $2\theta$ .

Some properties of crystal that could be measured by XRD are lattice parameter, phase identity, phase purity, crystallinity, crystal structure, and percent phase composition. Meanwhile, the benefits that could be obtained are non-destructive, fast, and easy sample preparation. High accuracy for d-spacing calculations could be used for single crystal, poly crystal and amorphous materials. The standards are already available for thousands of material systems.

#### A.6. Raman Spectroscopy

When light interacts with matter, the photons which make up the light might be scattered or absorbed. It is also possible for the photon not to interact with the materials but simply pass through it. However, if the energy of the photon corresponds to the energy gap between the ground state of a molecule and the excited state, the photon might be absorbed and the molecule would be promoted to the higher energy excited state. In this case, the

loss of radiation energy of the photon is measured in absorption spectroscopy. But if the energy of the photon doesn't match the energy gap between two levels of energy state, the photon would scatter from the molecule. In Order to measure the scattered photons, light would be collected at an angle to the incident light beam and make sure that there is no absorption from any electronic transition which have similar energies to that of the incident light.

Basic principles of Raman spectroscopy is the detection of vibrations in molecule based on the process of infrared absorption and Raman scattering. The result from Raman spectroscopy could be used to determine the chemical structures and the physical forms, identify substances from the characteristic special patterns and determining quantitatively or semi quantitatively the amount of substance in a sample.[46]

#### **A.7. Solar Simulator**

Solar simulator is commonly used for measurement of energy output for a photovoltaic device. The energy output which is declared as Watt peak value, should be tested under a standard test conditions (STC). The watt-peak value could be obtained by using a current voltage (IV) characterization with a help of variable load while the PV device is illuminated by light. The reliability of this value and its associated uncertainty are definitely important to manufacturers, operator, and investors. Each measurement has to demonstrate an unbroken traceability chain to international primary standards and calculation of measurement uncertainty for each transfer in the chain.

The STC of a photovoltaic device measurement has been defined in an international standard (IEC 60904) as the temperature of the module should be 25°C. The air mass condition is 1.5 (AM1.5) and total irradiance of 1000W/m<sup>2</sup> with a specific spectral irradiance that has been determined.

#### **A.8. External Quantum Efficiency**

Quantum efficiency (QE) measurement is one of the most important methods to quantify the efficiency of the conversion of light to electron as function of wavelength. The QE measurement is an indicator of how good a solar cell at converting sun light into electricity. If all photon of certain wavelength are absorbed and all of the minority carriers that generated could be collected, then the quantum efficiency at that particular wavelength is 100%. The quantum efficiency for photons below the band gap is zero. But in fact, it is very difficult for a solar cell to achieve 100% quantum efficiency. It is due to recombination, optical loss like reflection, and parasitic absorption.

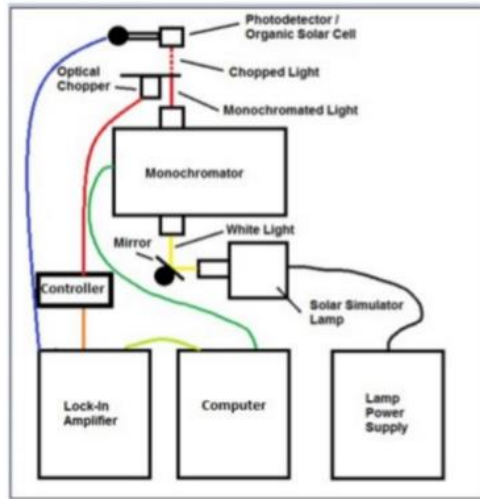


Figure 36. Schematic of EQE measurement

The principle of EQE measurement is based on illuminating of a sample by monochromatic light and recording the electrical (number of generated carriers) output from sample. By varying the wavelength of the light source, the entire EQE curve could be established. The integration of the area under the curve would give the current density ( $J_{SC}$ ). The EQE measurement consists of several components such as a light source, monochromator, a lock in amplifier, and a chopper. Schematic of an EQE measurement setup could be found in figure 36. In the measurement, solar cell was illuminated by monochromatic light which controlled by monochromator. A mechanical chopper modulates the probe beam at 123Hz. Before starting the measurement, calibration using a device which response is already known should be done. After finishing the calibration, the EQE and  $J_{SC}$  could be calculated by using equation 9

$$\mathbf{EQE}(\lambda) = \mathbf{EQE}_{\text{ref}}(\lambda) \times \frac{\mathbf{I}(\lambda)}{\mathbf{I}_{\text{ref}}(\lambda)} \quad (9)$$

- Where:
- $\mathbf{EQE}(\lambda)$  = External Quantum Efficiency of the sample (%)
  - $\mathbf{EQE}_{\text{ref}}(\lambda)$  = External Quantum Efficiency of the calibrator (%)
  - $\mathbf{I}(\lambda)$  = Current generated by the sample (mA)
  - $\mathbf{I}_{\text{ref}}(\lambda)$  = Current generated by the calibrator (mA)

While for calculating  $J_{SC}$

$$\mathbf{J}_{SC} = -\mathbf{q} \int_{\lambda_1}^{\lambda_2} \mathbf{EQE}(\lambda) \phi_{\text{ph},\lambda}^{\text{AM1.5}} \mathbf{d}\lambda \quad (10)$$

- Where:
- $\mathbf{J}_{SC}$  = Current density ( $\text{mA}/\text{cm}^2$ )
  - $\phi^{\text{AM1.5}}$  = Photon flux in AM 1.5 spectrum

### A.9. Photon Annihilation Spectroscopy (PAS)

Photon Annihilation Spectroscopy (PAS) is known as powerful equipment to investigate microstructure of condensed matter. It could be used to characterize various kind of material such as metals, alloys, semiconductors and macromolecular solids. Positron ( $e^+$ ) is the antiparticle of electron ( $e^-$ ). The annihilation between positron and electron due to their electromagnetic interaction would creates the total energy of 1.022MeV, corresponding to the combined rest ass energies of the positron and electron. The energy is released in forms of photons. The number of photons depends on how the positron and electron annihilate. The mass would be transformed into photon if the particles have a low energy. In the most cases two  $\gamma$ -quanta would appear according to equation 11



Pair of  $\gamma$ -quanta have their own energy from the result of positron-electron annihilation. The energy of pair of  $\gamma$ -quanta could be described as

$$E_{2\gamma} = 2m_0c^2 + E_{e^-} + E_{e^+} \quad (12)$$

Where:  $E_{2\gamma}$  = Energy of 2  $\gamma$ -quanta  
 $E_{e^-}$  = Energy of electron  
 $E_{e^+}$  = Energy of positron

Where  $m_0c^2 = 0.511$  MeV. There are several ways to generate a positron. The most common two of them are from isotope source or by pair production. Most of the study by using PAS have been using isotope from  $^{22}\text{Na}$ ,  $^{58}\text{Co}$ ,  $^{64}\text{Cu}$ , and  $^{68}\text{Ge}$ . However Na is one of the most favorite isotopes, since it has long life, short biological half-life, relatively cheap, effective, and easy to handle since it's available in a dilute  $^{22}\text{NaCl}$  solution. Figure 37 shows the scheme decay of  $^{22}\text{Na}$ . Equation 11 shows the decay reaction of  $^{22}\text{Na}$ .

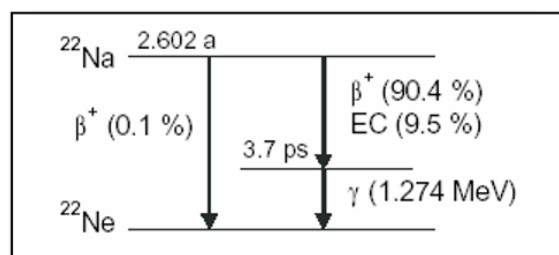
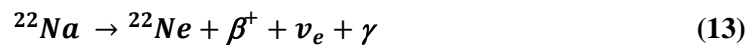


Figure 37. Schematic process in Positron generation from Natrium decay [47]

It could be seen from the scheme, that  $^{22}\text{Na}$  isotopes gives a relatively high positron yield of 90.4%. The positron emission is almost simultaneous with the emission of  $\gamma$ -ray which has energy of 1.274MeV. This simultaneous reaction could be used as a start event for lifetime spectroscopy. Pair-production positron source use high energy  $\gamma$ -rays beams spontaneously to create a positron and an electron. Positron beam typically has energy between 10eV to 100keV.

There are several experimental techniques which are included in a PAS measurement, they are positron lifetime spectroscopy, angular correlation annihilation radiation, Doppler broadening spectroscopy, and age-momentum correlation. The 4 experimental techniques could be explained by figure 38.

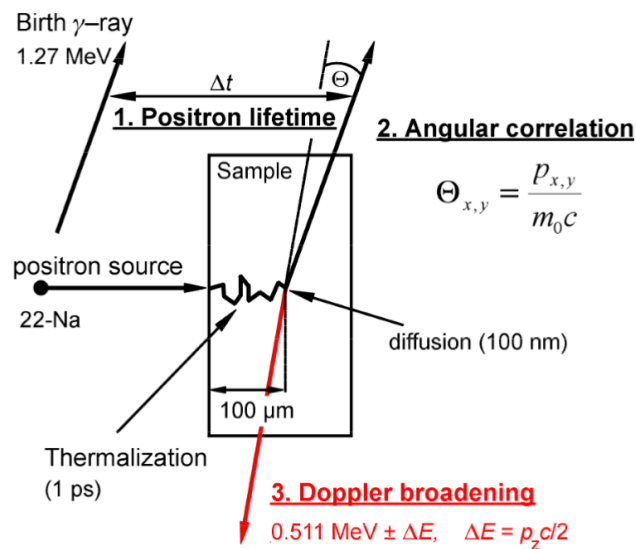
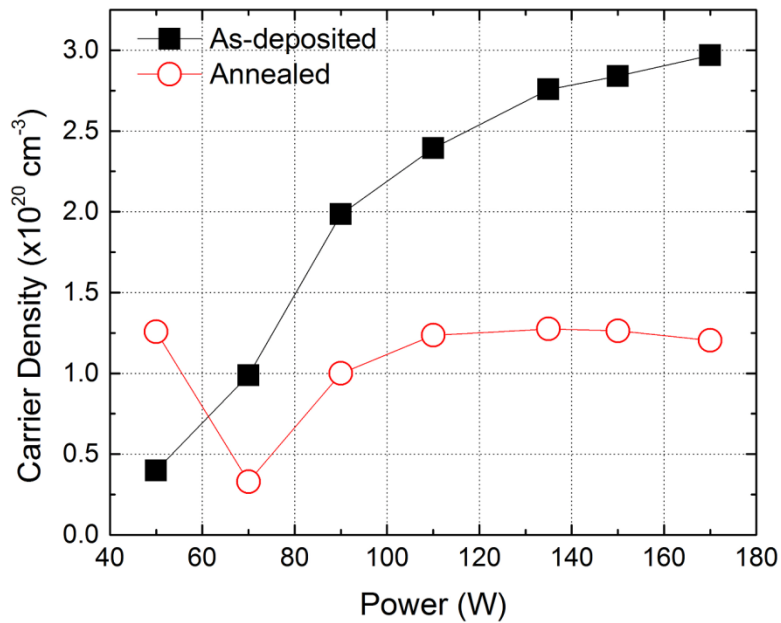
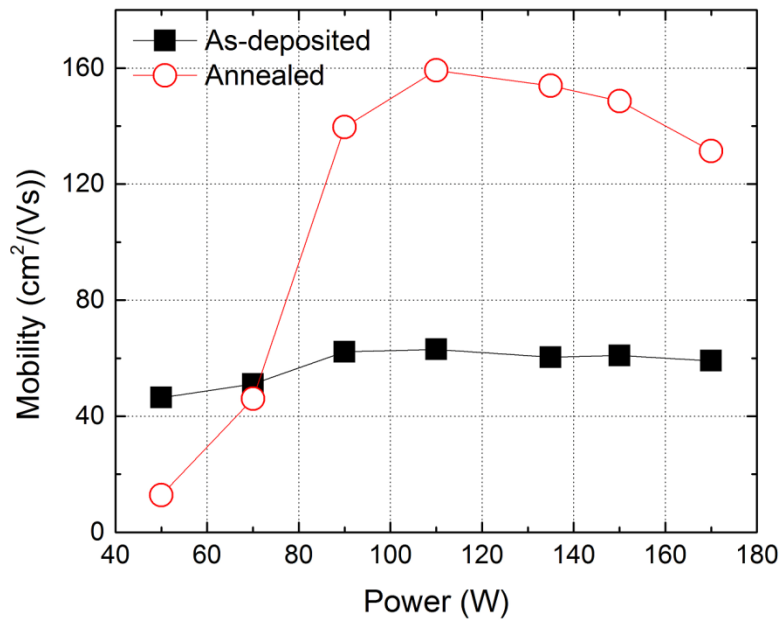


Figure 38. Illustration of Photon Annihilation spectroscopy measurement [48]



## Appendix B

### Electrical Properties of IO:H layer for different Power



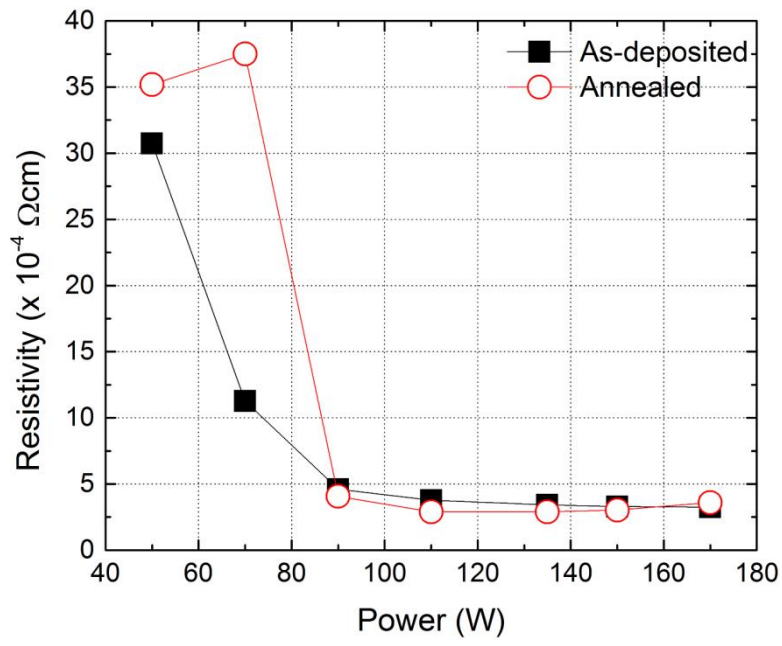


Figure 39. Mobility, carrier density, and resistivity of IO:H layer for different power

## Appendix C

### Water vapor effect on different thickness of IO:H

From Chapter 3.3, it is known that for thickness above 200 nm, the mobility of the sample cannot exceed  $120 \text{ cm}^2/\text{Vs}$ . The result was obtained by the optimum water vapor for sample with 100nm thickness. Therefore the effect of water vapor for different thickness should be observed.

#### C.1. IO:H Layer with 200nm Thickness

##### C.1.1. Electrical Properties

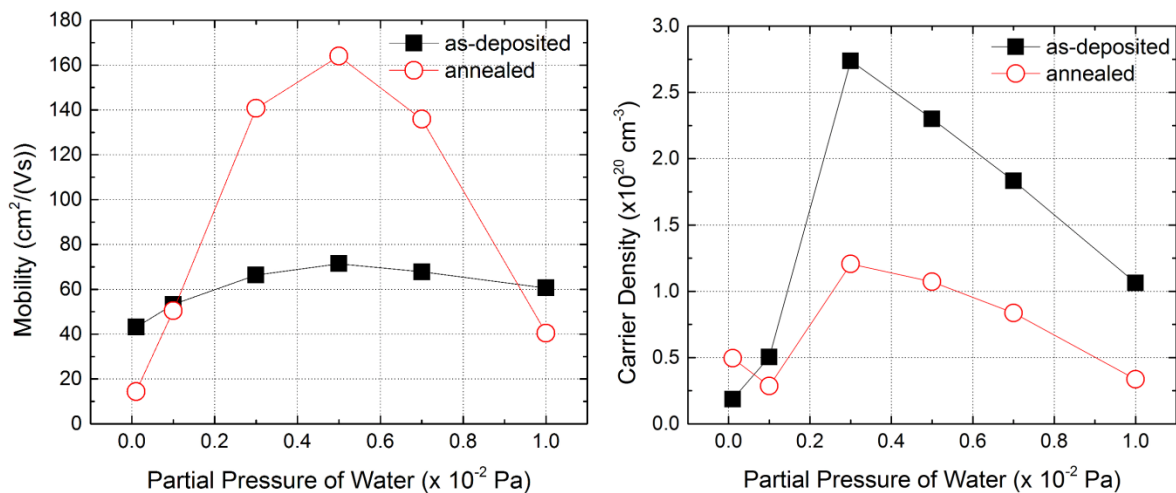


Figure 40. a. Mobility and b. Carrier density of IO:H layer with thickness of 200nm for different partial pressure of water

From figure 40 it can be seen that the optimum mobility of the layer was not at the partial pressure of water  $3 \times 10^{-3} \text{ Pa}$ , but shifted to higher partial pressure of water. In the as deposited sample, it shows similar behavior that the mobility seems to reach maximum point at around  $60 \text{ cm}^2/\text{Vs}$ . But the result in carrier density shows that the highest carrier density was obtained at same water vapor as 100nm thickness IO:H. The result after the annealing shows that the layer with partial pressure of water vapor at  $1.00 \times 10^{-3}$  and  $1.00 \times 10^{-2} \text{ Pa}$  did not increase the mobility of the layer. The carrier density of the layer shows that after the annealing, it will always drop. However the sample with no water vapor and  $1.00 \times 10^{-3} \text{ Pa}$  water vapor during deposition shows increase in carrier density and just a little bit decrease in carrier density respectively.

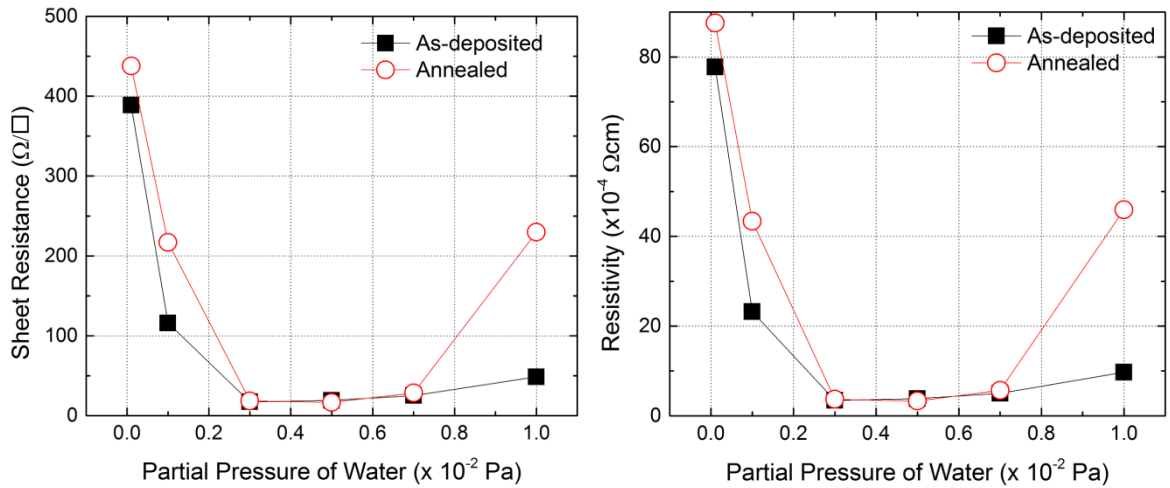
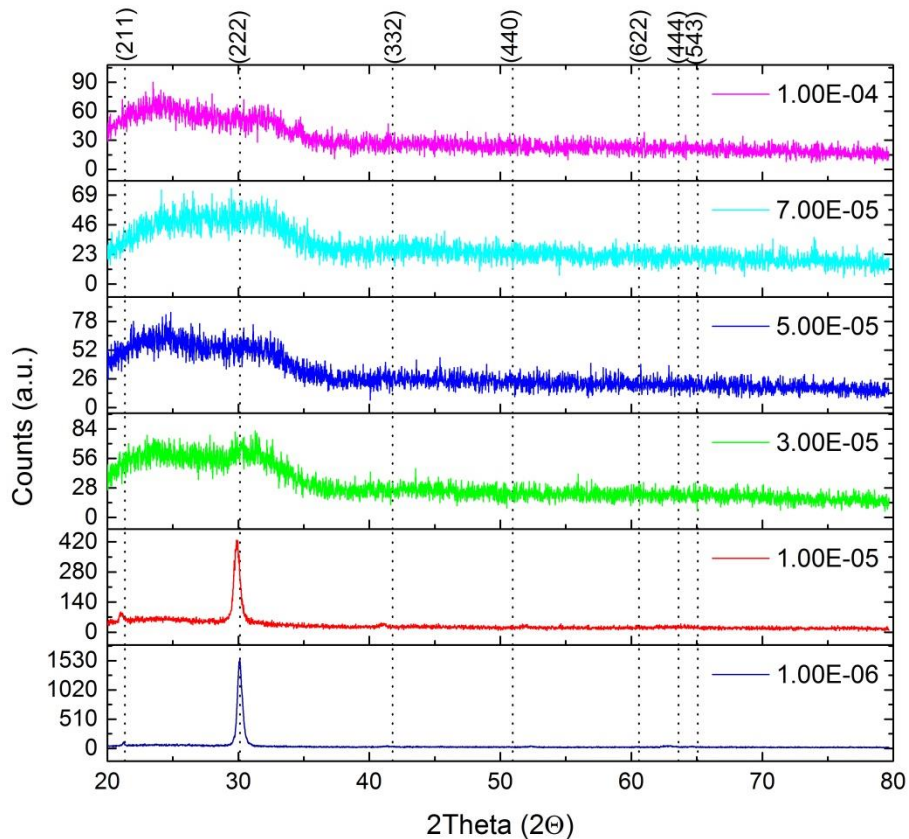
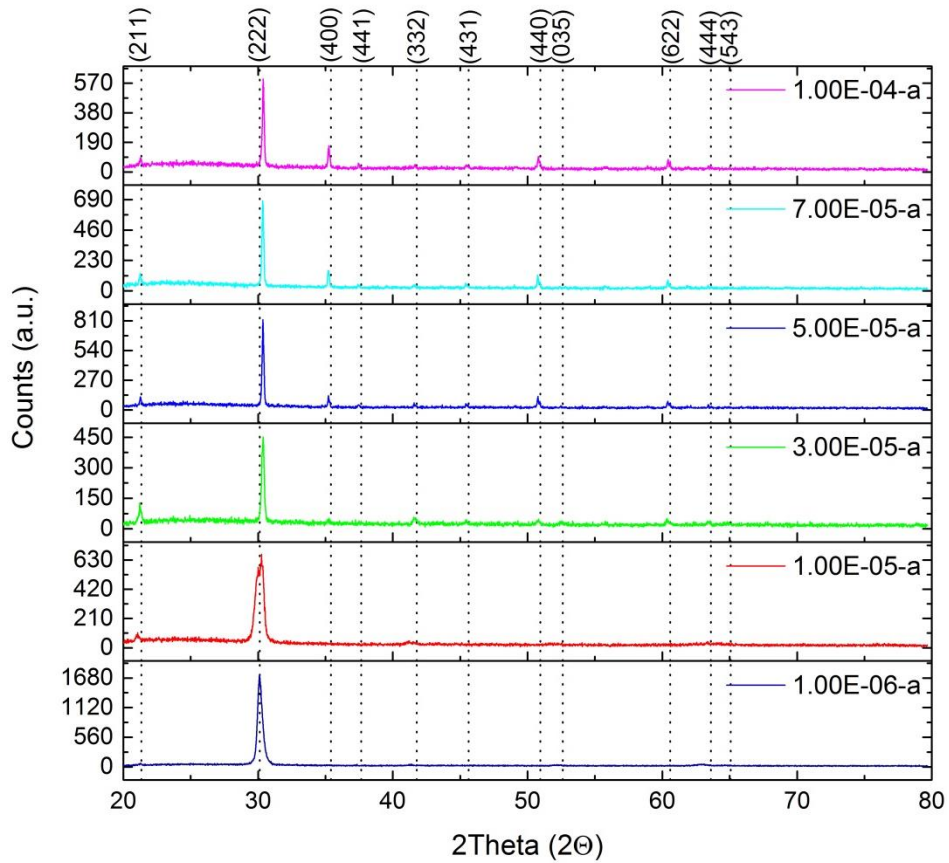


Figure 41. Resistivity and sheet resistance of IO:H layer with thickness of 200nm for different partial pressure of water

The figure 41 shows the resistivity result of the layer, in general, the resistivity of the layer will increase after the annealing. This result was due to the drop in the carrier density outweigh the increase in mobility, except for the sample with partial pressure of water  $5.00 \times 10^{-3}$  Pa. The sheet resistance of the samples which shown in figure 38 indicate that the lowest sheet resistance that could be obtained from the layer is between  $16 \Omega/\square$  to  $19 \Omega/\square$ .

### C.1.2. XRD Characterization





**Figure 42. XRD characterization of IO:H layer with thickness of 200nm for different partial pressure of water a. as deposited and b. annealed**

Figure 42 shows XRD characterization result of the as-deposited and annealed sample respectively. The sample with no water vapor during deposition and the sample with partial pressure of water at  $1.00 \times 10^{-3}$  mbar were crystalline in the as deposited. After the annealing, all of the samples turned out to be crystalline. All of the sample which in amorphous phase in the as-deposited sample, and turn to crystalline after the annealing experience drop in the carrier density. Calculation with scherrer method to understand the layer has been done.

Table 10. XRD calculation for IO:H layer with thickness of 200nm

Partial Pressure of Water (Pa)	FWHM (°)	Peak position (2θ)	Particle Size (nm)
<b>as-deposited</b>			
$1 \times 10^{-4}$	0.4295	30.43	22.4067
$1 \times 10^{-3}$	0.5539	30.17	17.3263
<b>annealed</b>			
$1 \times 10^{-4}$	0.4112	30.43	23.3998
$1 \times 10^{-3}$	0.704	30.59	13.6909
$3 \times 10^{-3}$	0.2123	30.69	45.438
$5 \times 10^{-3}$	0.1509	30.67	63.9252
$7 \times 10^{-3}$	0.15	30.65	64.2937
$1 \times 10^{-2}$	0.1598	30.69	60.3647

The calculation shows that after the annealing, the sample which deposited in an amorphous state, and crystallized will have bigger particle size, compared to sample which deposited directly in the crystalline phase. The bigger particle size might be the reason of high mobility of the sample. However, the sample which deposited with vapor at  $1.00 \times 10^{-3}$  Pa, this might be during the first 100 nm deposition, high partial pressure of water create too much void inside the layer, which turned out to decrease the mobility instead of increase it.

## C.2. IO:H Layer with 400nm Thickness

### C.1. Electrical Properties

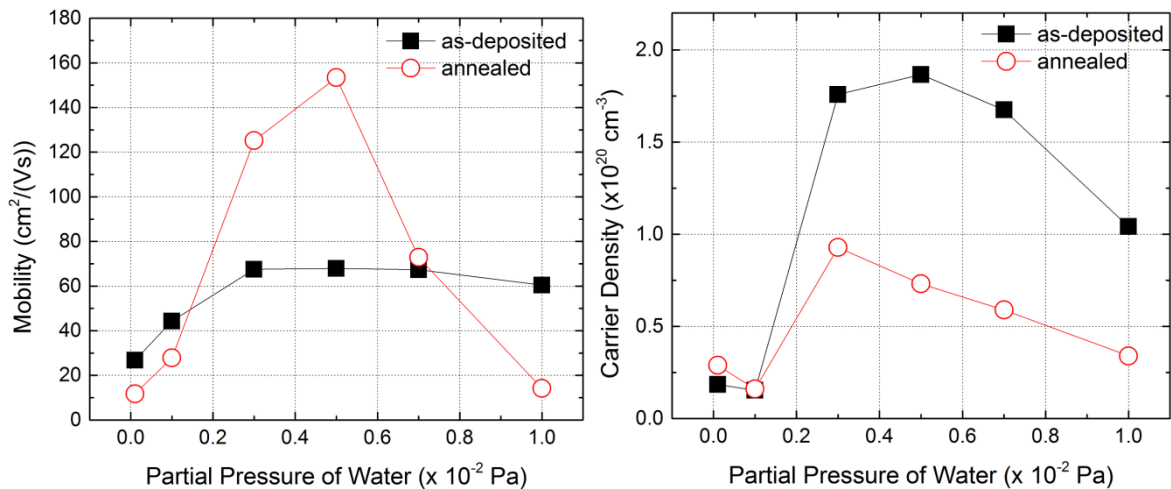
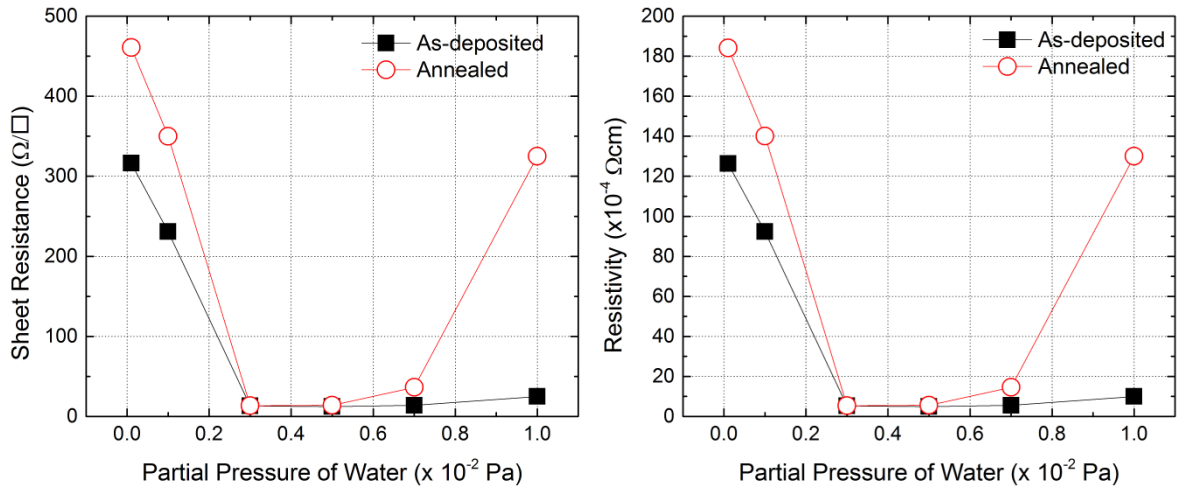


Figure 43. a. Mobility and b. carrier density of IO:H layer with thickness of 400nm for different partial pressure of water

Figure 40 shows that once again, the mobility of the as-deposited sample limited by  $65 \text{ cm}^2/\text{Vs}$ . While the carrier density shows different result for the sample with different thickness. The maximum carrier density of the layer was obtained when water vapor with

partial pressure of  $5.00 \times 10^{-5}$  was introduced during deposition. After the annealing, the mobility shows an interesting change. Samples with no water during deposition and very low water vapor have lower mobility after the annealing. Moreover, the sample with very high partial pressure of water experiences a drop in mobility. Figure 40 shows that after the annealing, carrier density of the sample with no water vapor introduced during deposition will increase.



**Figure 44. a. Resistivity and b. sheet resistance of IO:H layer with thickness of 400nm for different partial pressure of water**

Figure 44 shows the resistivity and sheet resistance of as deposited and annealed IO:H layer respectively. As expected, there will be a huge drop in the resistivity when the water vapor was increased from  $1.00 \times 10^{-3}$  Pa to  $3.00 \times 10^{-3}$  Pa since the carrier density of the as-deposited sample has big difference. Overall, the resistivity of the sample increase after the annealing, which caused by the drop of carrier density outweigh the increase in mobility. The sheet resistance of the IO:H layer can reach as low as  $12.5 \Omega/\square$  with the partial pressure of water at  $5.00 \times 10^{-3}$  Pa. However, from the point of view of conductivity, annealing doesn't provide so much for layer with 400 nm thickness.

## C.2. XRD Characterization

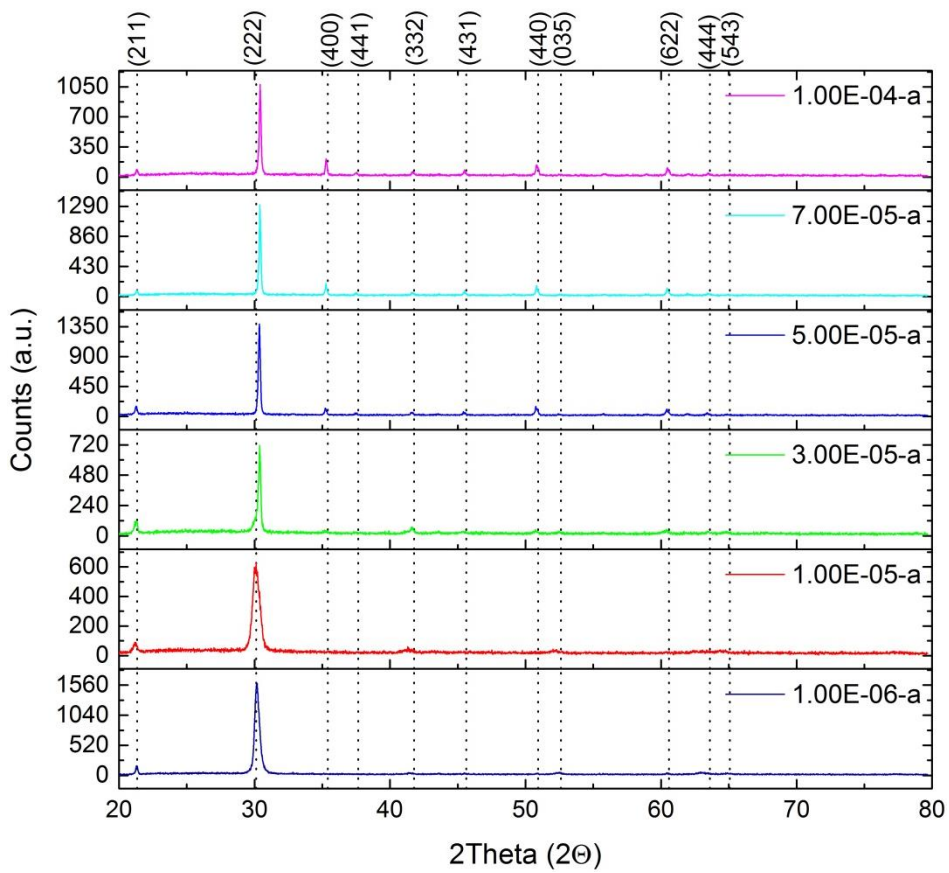
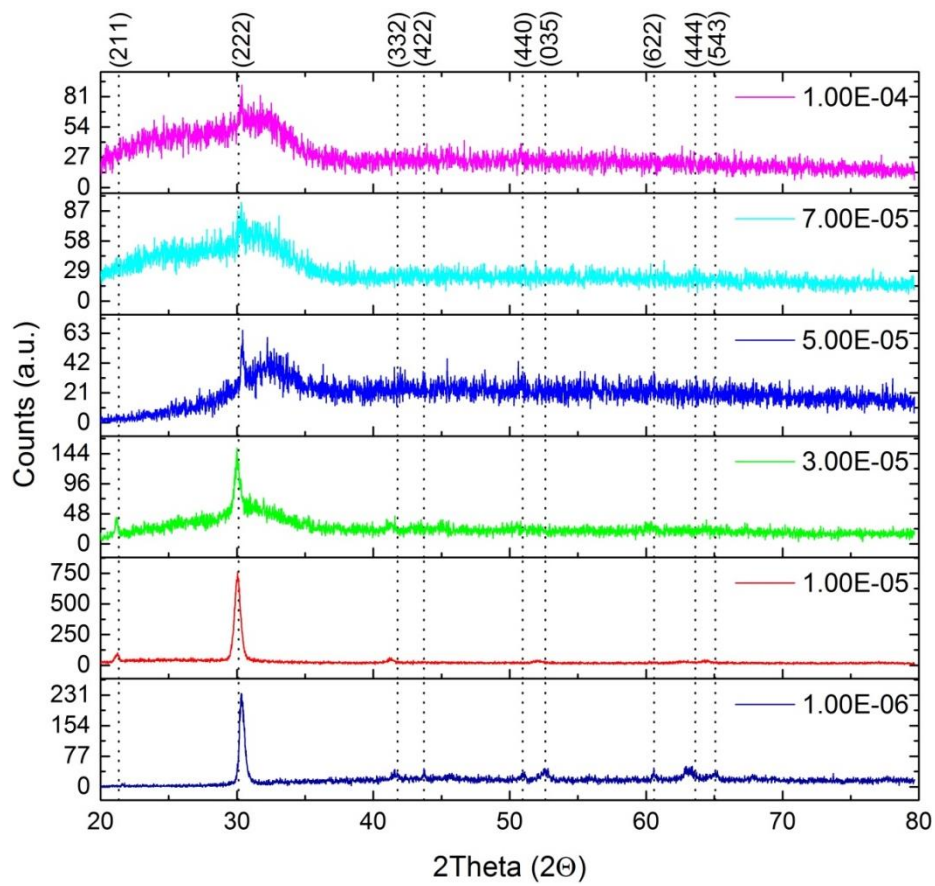


Figure 45. XRD characterization for IO:H layer with 400nm thickness with different partial pressure of water a. as-deposited and b. annealed

Figure 45 shows the XRD result for the as-deposited and annealed layer with 400nm thickness. The results are very different from the sample with 100 nm and 200 nm thickness. For sample with 400 nm thickness, XRD characterization can detect a peak in all of the as-deposited sample. However, the peak signals are very weak which lead the calculation of the particle size become so difficult to be done. After the crystallization, all of the samples become fully crystalline. Samples with low peak signal in the as-deposited layer has more random orientation compared to sample which already polycrystalline during deposition.

**Table 11. XRD calculation for IO:H layer with 400nm thickness**

<b>Partial Pressure of water (Pa)</b>	<b>FWHM (2<math>\theta</math>)</b>	<b>Peak Position (2<math>\theta</math>)</b>	<b>Particle Size (nm)</b>
<b>as-deposited</b>			
<b>1 x 10<sup>-4</sup></b>	0.4054	30.63	23.7832
<b>1 x 10<sup>-3</sup></b>	0.5121	30.37	18.7803
<b>3 x 10<sup>-3</sup></b>	0.5558	30.33	17.2946
<b>annealed</b>			
<b>1 x 10<sup>-4</sup></b>	0.4103	30.47	23.4619
<b>1 x 10<sup>-3</sup></b>	0.6529	30.45	14.7428
<b>3 x 10<sup>-3</sup></b>	0.1973	30.69	48.9114
<b>5 x 10<sup>-3</sup></b>	0.1604	30.67	60.1453
<b>7 x 10<sup>-3</sup></b>	0.1469	30.71	65.6679
<b>1 x 10<sup>-2</sup></b>	0.1615	30.73	59.7565

From the calculation using scherrer equation, the particle size of the sample can be calculated. All of the sample with amorphous phase during deposition will experience an increase in particle size. However, there is a thing to notice, even though the particle size was increased, in some of the sample the mobility was decreased. It is something that shows the grain boundaries is not the one that limits the mobility of the sample.